diamagnetic zinc(II) complex is helpful in recording the 2D NMR data. Their reactivities and considerations about electronic structures complete this chapter.

References are grouped together at the end of this thesis.

Chapter II

Copper (II,I)-pterin coordination chemistry with a 6-substituted pterin ligand: synthetic, characterization and reactivity studies including utilization of molecular oxygen (O_2) for organic substrate conversion.

Abstract

A 6-substituted pterin ligand 2-amino-7-methyl-4-oxidopteridine-6-carboxylic acid (**1**, H_2L) plays a pivotal role for the present study; it is complemented by a π-acid ligand like 1, 10-phenanthroline (phen). Solubility of **1** in aqueous alkali permits the synthesis of a mononuclear copper(II) complex $[Cu^{II}(L)(phen)(H_2O)].\ 3H_2O$ (**2**) from this medium in the crystalline form and its x-ray structural characterization (CCDC deposition no. 985054; $R[F^2>2\sigma(F^2)]=0.113$; $wR(F^2)=0.279$). Alternatively, the green crystals of **2** can also be obtained through a redox cycle involving the $NaBH_4$ reduction of **2** and the aerial reoxidation of the resulting dark-brown

compound. Such crystals provide x-ray structural data of better accuracy ($R[F^2>2\sigma(F^2)]=0.051$; $wR(F^2)=0.136$; Baisya, S. S.; Roy, P. S. Acta Cryst. **2014**, E70, 348 – 351)[17b]. The above-mentioned dark-brown compound $Na_2[Cu^{I}(L')(H_2O)_2\text{-}\mu\text{-}(phen)\text{-}Cu^{I}(L')(H_2O)_2].\ 2H_2O$ (**3**), can be isolated in the solid state, where $(L')^{2-}$ is the 7,8-dihydro form of $(L)^{2-}$. Characterization data (elemental analysis, spectroscopy and electrochemical studies) of both **2** and **3** are presented here. The DFT optimized molecular structure of **3** affords realistic geometry parameters and helps to rationalize its physico-chemical/spectroscopic data. Reactivity of **2** towards both imidazole and $NaBH_4$ have been followed kinetically; the relevant negative $\Delta S^{\ddagger}$ values indicate the associative nature of the reaction pathways. The reaction of **2** with $NaBH_4$ turned out to be a two-step process, which can be rationalized from the thermodynamic considerations. Reaction of **3** with bromobenzene in presence of dioxygen has been followed both kinetically and stoichometrically; isolation and characterization of 4-bromophenol as a product of this reaction, point towards aromatic ring activation. Attempts have been made to correlate some of the above reactivities with the electronic structures of **2** and **3**, obtained by DFT calculations. The exceptionally small band gaps (ΔE = 0.22 – 0.5 eV) between the LUMO and LUMO+1 levels of **2** and that between the HOMO – 1 and HOMO – 2 levels of **3** respectively, are noteworthy. Such a situation is beneficial for accommodating the reducing equivalents transferred by $NaBH_4$ towards **2** leading to the formation of **3**; the latter responds either to a reaction mixture of bromobenzene and dioxygen or aerial oxidation, with the recovery of **2** as one of the products. This facile interconversion of **2** and **3**, is believed to be associated with the stability (both molecular and electronic structures) of **2**; the combined role of the redox non-innocent pterin ligand and the dual oxidation states (II, I) of the copper ion, in this process is highlighted.

Introduction

Pterins (2-amino-4-oxopteridines) are ubiquitous in nature including different classes of metalloenzymes containing molybdenum or tungsten or iron (nonheme or heme). [1 – 8,133]For such enzymes the redox non-innocent nature of pterin is reciprocated by the ability of the associated transition metal ion in displaying multiple oxidation states. Their functional aspects need the tacit assumption that the redox process at the metal centre should be linked to the changes in the pterin/pyrazine ring oxidation level.[9 – 11, 13]Such information have fostered a remarkable growth of pterin coordination chemistry.[10 – 18,142]

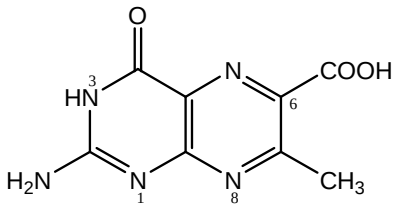

The pterin ligand (**1**, H_2L)

The phenylalanine hydroxylase (PAH) catalysed reaction is concerned with the insertion of one oxygen atom from molecular oxygen (O_2) into an aromatic ring, involving the C – H bond activation / hydroxylation[7]. On the other hand, copper-mediated oxidations cover a diverse array of reactions in both biology and chemistry [153] . Here the posisibility of developing a biomimic of the PAH enzyme is explored, utilizing the above versatility of coper-oxygen chemistry. Two new copper complexes of the 6-substituted pterin ligand, 2-amino-7-methyl-4-oxidopteridine-6-carboxylic acid (**1**, H_2L) assist this endeavour[17b]. The experimental designs involve their interfacing with the oxidized and reduced (dihydro) forms of the pterin ring, for developing the copper-pterin-O_2 chemistry.[10, 14, 18,137,139,153].

Experimental Section

General. All starting materials and solvents were purchased from reliable commercial sources and used without further purification. Electronic spectra and kinetic data were recorded on a

Jasco V-530 UV-vis spectrophotometer, with thermostatic conditions (±0.5K) being maintained using a Shimadzu (TB-85) thermostat. Infrared spectra were recorded on a Perkin Elmer model RXI infrared spectrophotometer. Some of the ^{1}H NMR spectral measurements were done on a Bruker, Avance 300 MHz NMR spectrometer. Fluorescence spectra were recorded on a Photon Technology International spectrofluorometer(model Fluorescence Master System). Magntic susceptibility measurements were performed on a Sherwood instrument (model MSB mk1), using $HgCo(SCN)_4$ as the calibrant. Cyclic voltammetric experiments were performed with a Bioanalytical Systems Epsilon electrochemical workstation (model CV-50) using 1.0mM analyte in DMSO (0.1 M TBAP; glassy carbon working electrode). Elemental analysis data, some of the mass spectra, 500 MHz ^{1}H NMR spectral data, CD spectral data and X-ray diffraction data were obtained from CSMCRI, Bhavnagar. EPR and rest of the mass spectral data were recorded by SAIF, IIT, Bombay and SAIF, CDRI, Lucknow, respectively.

Computational Details. DFT calculations were done using the GAUSSIAN 09 and GAUSS VIEW 5 program packages. For **2** the XRD structure was used as the starting point. Geometry optimizations were done with the DFT-B3LYP approach using the 6-31G* basis set[155-159]. For **3** the optimized structure based on elemental analysis, ESIMS, IR, CD and ^{1}H NMR data was used for electronic structure calculation.

Synthesis of 2-amino-4-hydroxy-7-mthylpteridine-6-carboxylic acid sesquihydrate($H_2L.1.5H_2O$) (1). It was obtained by a published procedure[19]. Yield : moderate. Anal. Calcd for $C_8H_7N_5O_3$. $1.5H_2O$: C, 38.71; H, 4.03; N, 28.22. Found : C, 38.96; H, 3.18; N, 28.0.

Synthesis of [Cu^{II}(L)(phen)(H_2O)]. $3H_2O$ (2). This compound could be prepared by altarnative methods, e.g., **method A** and **method B** respectively, as described by Baisya and Roy[17b]. Brief outlines of such procedures are presented below.

Method A. This procedure involves a reaction on the 0.125mmol scale in aqueous alkaline medium (50mL, pH10.5) among $Cu(NO_3)_2.3H_2O$, 1, 10-phenanthroline monohydrate (phen) and the pterin ligand **1** dissolved in NaOH (0.275mmol); a steady flow of dixyygen is to be maintained for 60h at 301-303K under subdued light. The final blue solution yielded green crystals within a week [Figure II- 1(a) and (b)]. Their x-ray structural data are available from the Cambridge Crystallographic Data Centre (CCDC deposition No. 985054). (Anal. Calcd for $CuC_{20}H_{21}N_7O_7$: C, 44.89; H, 3.93; N, 18.33. Found C, 43.38; H, 4.06; N, 17.65).

Method B. Treatment of **2** (obtained by **Method A**) with equimolar amount (0.125mmol scale) of $NaBH_4$ in aqueous medium (50mL) at 301-303K, produced a dark-brown compound [Figure II-1(c)]. Subsequent aerial exposure reoxidized this reduced complex affording the above-mentioned green crystals (**2**) again [Scheme II- 8(a)], which were also characterized x-ray structurally[17b].This dark-brown compound could be isolated in the solid state, by repeating this reaction in CH_3OH medium, using an excess of $NaBH_4$, as described below.

Synthesis of $Na_2[Cu^I(L')(H_2O)_2$-μ-(phen)-$Cu^I(L')(H_2O)_2]$. $2H_2O$ (3), where $(L')^{2-}$ is the 7,8-dihydro form (Scheme II-4) of the pterin ligand anion (Scheme II-1); chemical composition of **3** was established on the basis of microanalytical and spectroscopic data (vide infra). A methanolic solution (50 mL) of **2** (26.7 mg, 0.05 mmol) was treated with $NaBH_4$ (11.3 mg, 0.3 mmol) and the reaction was allowed to continue for 45 min at 301-303K under subdued light in a Schlenk flask attached to a paraffin oil bubbler. The reaction mixture passed through a sequence of color changes e.g., bright green→pink→deep orange-brown. It was then rotavapped and a dark brown solid was recovered (Schemes II-5 and II-6). It was washed quickly (decantation) with dinitrogen purged CH_3OH (3 X 4 mL) and dried in vacuo over silica gel for 48h.Yield: 35%.

Anal. Calcd for $Na_2Cu_2C_{28}H_{34}N_{12}O_{12}$: C, 37.21; H, 3.80; N, 18.60. Found: C,36.98; H, 3.49; N, 17.58.

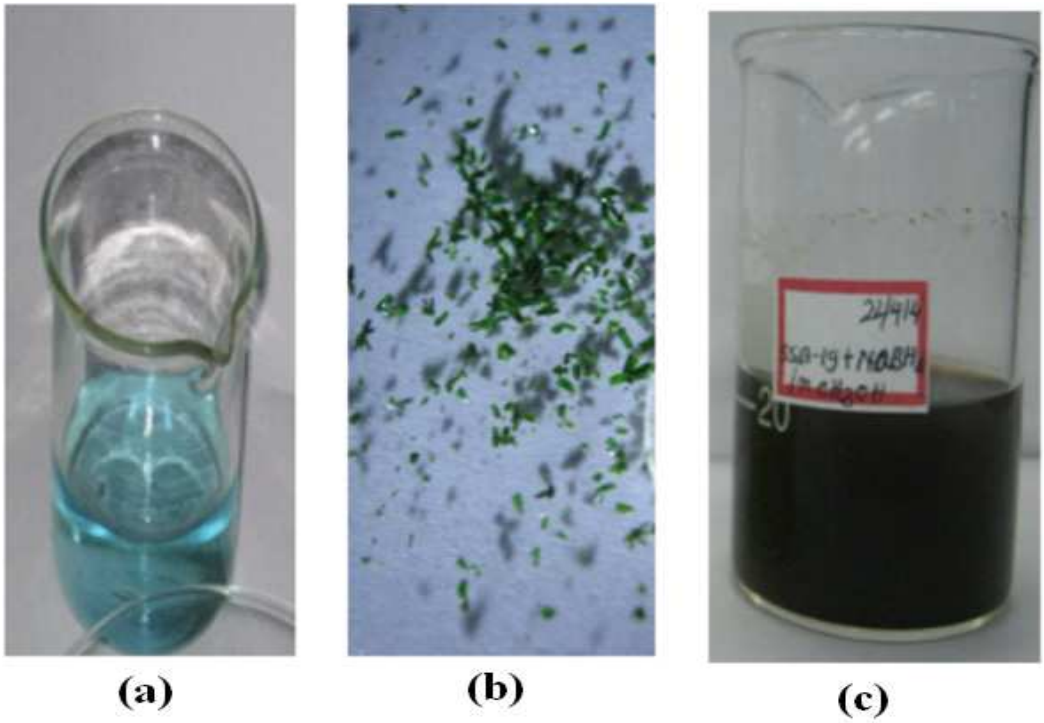

Figure II-1. The blue mother liquor (a) and the green crystals (b) as per method A[17b] ; (c) the dark-brown compound formed on treatment of **2** with equimolar amount of $NaBH_4$ in aqueous medium as described in method B[17b].

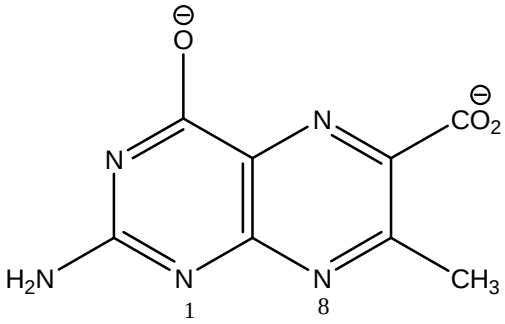

The pterin ligand (**1**, H_2L) anion (L^{2-})

Scheme II-1

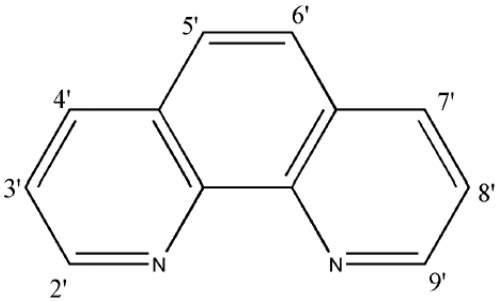

(phen)

Scheme II-2

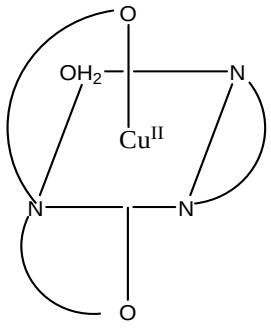

2

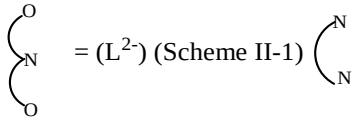

Scheme II-3

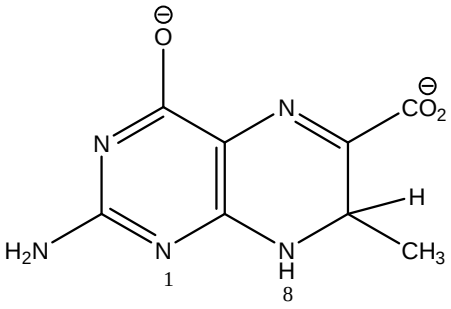

7, 8-dihydro form of the pterin ligand anion $(L')^{2-}$

Scheme II-4

Reaction of bromobenzene with 3 and the recovery of 4-bromophenol as well as 2 from the reaction medium [Scheme II- 8(b)]. For this purpose **3** was generated in situ from **2** and $NaBH_4$ and then reacted with bromobenzene, for completing the reaction sequence as outlined in Scheme II-8(b). Initially a methanolic solution (50 mL) of **2** (67 mg, 0.125 mmol) was reacted with $NaBH_4$ (47 mg, 1.25 mmol) under the aforesaid conditions. Next a methanolic solution (10 mL) of bromobenzene (196 mg, 1.25 mmol) saturated with dioxygen was added to the above reaction mixture, dioxygen was bubbled in for 2.5h and then left aside for 72h. After that the reaction mixture was rotavappd to dryness and extracted with pet ether (bp.313-333K). The pet ether extract was rotavapped to dryness yielding a white solid which was dried in vacuo over silica gel for 48h; m.p. 335K (literature data show a melting point of 337K for 4-bromophenol)[20]. IR data (nujol, cm^{-1}): new vibrational modes (with respect to bromobenzene) appear at 3350 [ν(OH)], 1333[δ(OH)] and 1285[ν(C-O) +δ(OH)] respectively, for the above white product, assignable to the phenolic – OH group[21]. In the ^1H NMR data [δ, $CDCl_3$, Me_4Si; Figure II-2] for bromobenzene over the region δ10.0 – 6.5, only two multiplet singnals (2:3 ratio) appear at δ7.48

and δ7.24 respectively, assignable to its aromatic protons[Figure II-2(a)]; for the above white product a new broad singlet signal appears at δ 9.26 [phenolic – OH proton; Figure II-2(b)], in addition to the two multiplet signals (1:1 ratio) connected by cross peaks at δ8.32 and δ7.73 respectively (aromatic protons), verifying the hydroxylation of the aromatic ring of bromobenzene.

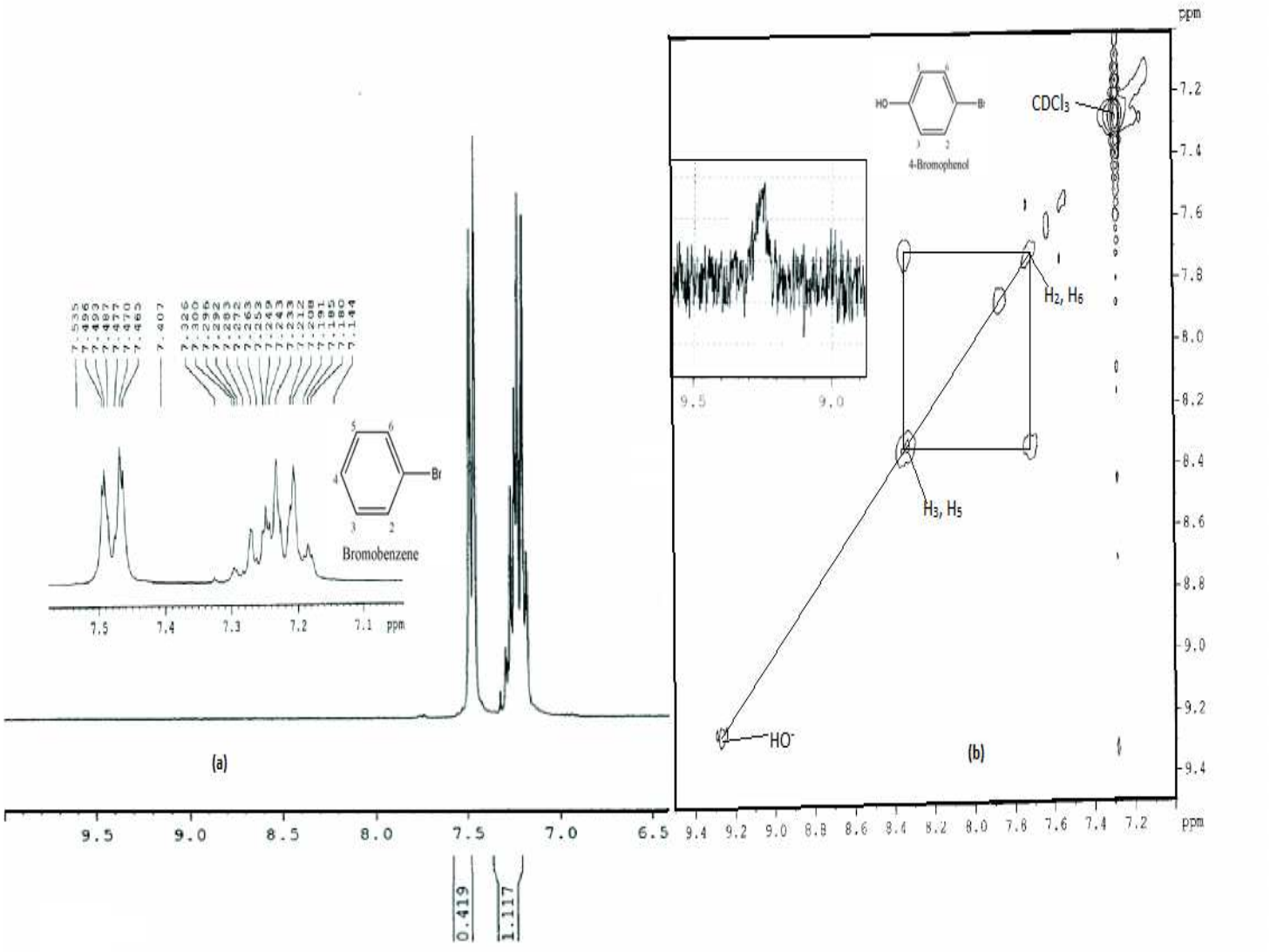

Figure II-2. (a) The 300 MHz ^{1}H NMR spectrum of bromobenzene in $CDCl_3$ over the region δ10 – 6.5. The inset shows the expanded view of the aromatic proton signals. (b) The 300 MHz

$^1H - ^1H$ cosy spectrum (symmetrized) of the recovered white compound (mp. 337K) (Schemes II-7, II-8) in $CDCl_3$ over the region δ9.5 – 7.0. The inset shows a new signal (- OH) at δ9.26 for this compound, as compared to the starting material bromobenzene.

The residual part of the above reaction mixture left behind after pet ether extraction, yielded a green product which could be purified (extraction with CH_3OH and recrystallization from the same solvent) and characterized. Its microanalytical data are similar to those of **2** (Anal. Calcd for $CuC_{20}H_{21}N_7O_7$: C, 44.89; H, 3.96; N, 18.33. Found C, 43.5; H, 3.4; N, 17.85). Further verification of its chemical composition is achieved from the mass spectral data (vide infra).

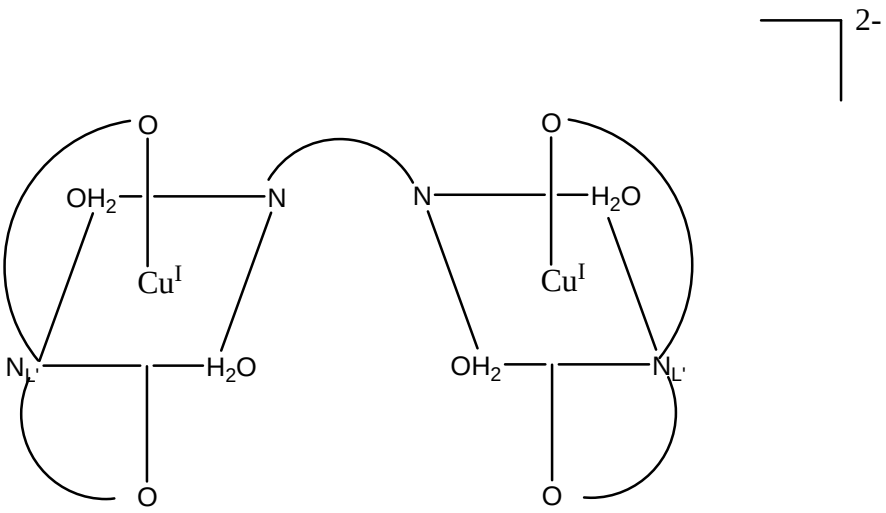

3

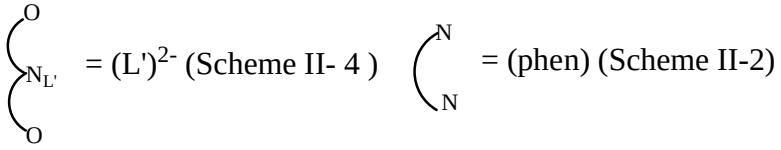

Scheme II-5

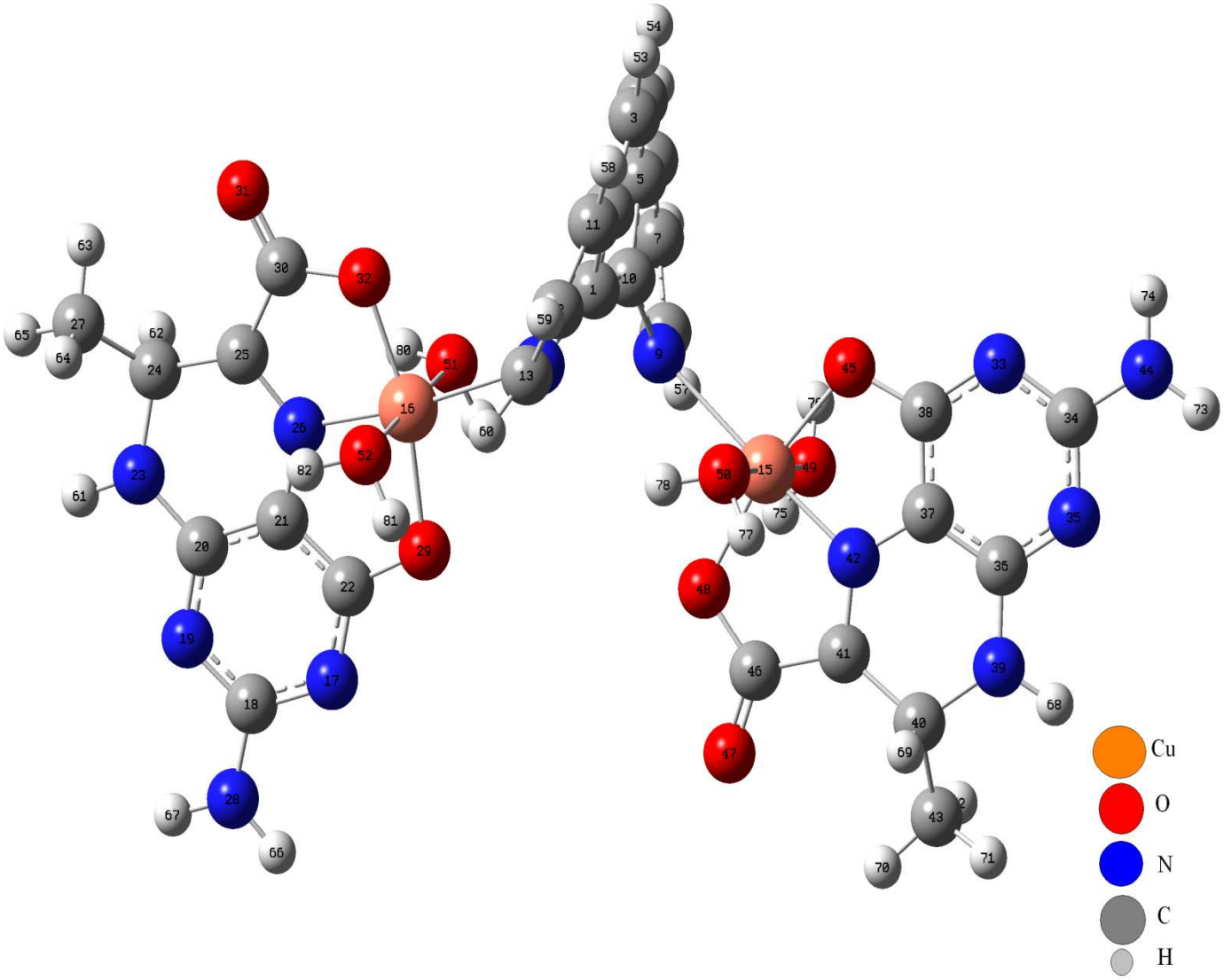

Scheme II-5(a) DFT optimized molecular structure of compound **3**; the Na^{+} ions are omitted for simplicity.

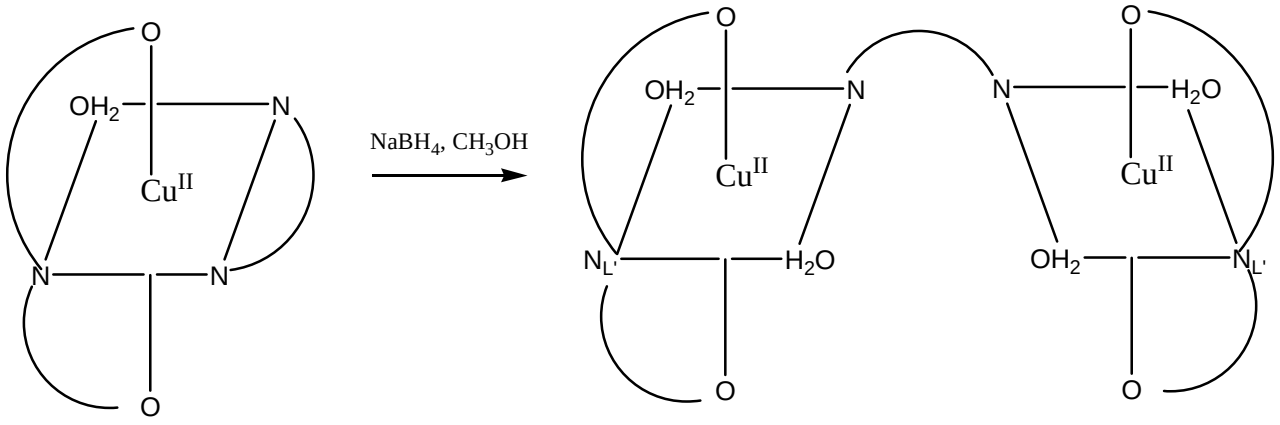

2, Scheme II-2 **2'**

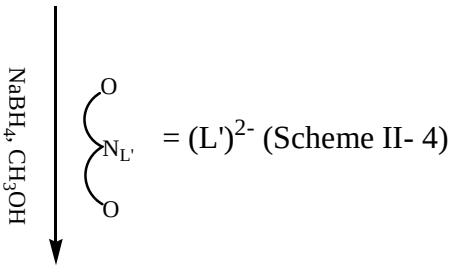

3, Scheme II-5

Scheme II-6

Bromobenzene bp. 430K —(**3**, O_2 / CH_3OH)→ 4-bromophenol mp. 337K

Scheme II-7

(a) **2** → **3** —(air)→ **2** (green crystals)

(b) **2** —($NaBH_4$ / CH_3OH)→ **3** —(O_2 / bromobenzene)→ **2** (green compound) + 4 - bromophenol

vide Schemes II-6 and II-7 for details

Scheme II-8

Results and Discussion

Synthesis of the complexes. It can be inferred from the experimental section that **2** can be synthesized by alternative routes, e.g., direct synthesis from a Cu(II) salt and the relevant ligands (method A), a redox reaction involving $NaBH_4$ reduction of **2** and its subsequent aerial reoxidation (method B) and finally its recovery from a reaction medium involving the interaction between **3** and bromobenzene [Scheme II-8(b)]. The above steps highlight the facile interconversion between **2** and **3** as well as the stability of the coordination geometry around the Cu(II) ion in **2**. Two of the above crops of **2** could be characterized x-ray structurally and the structural data of the one obtained using $NaBH_4$ reduction – aerial reoxidation cycle [method B, Scheme II-8(a)] are of better accuracy and summarized below[17b].

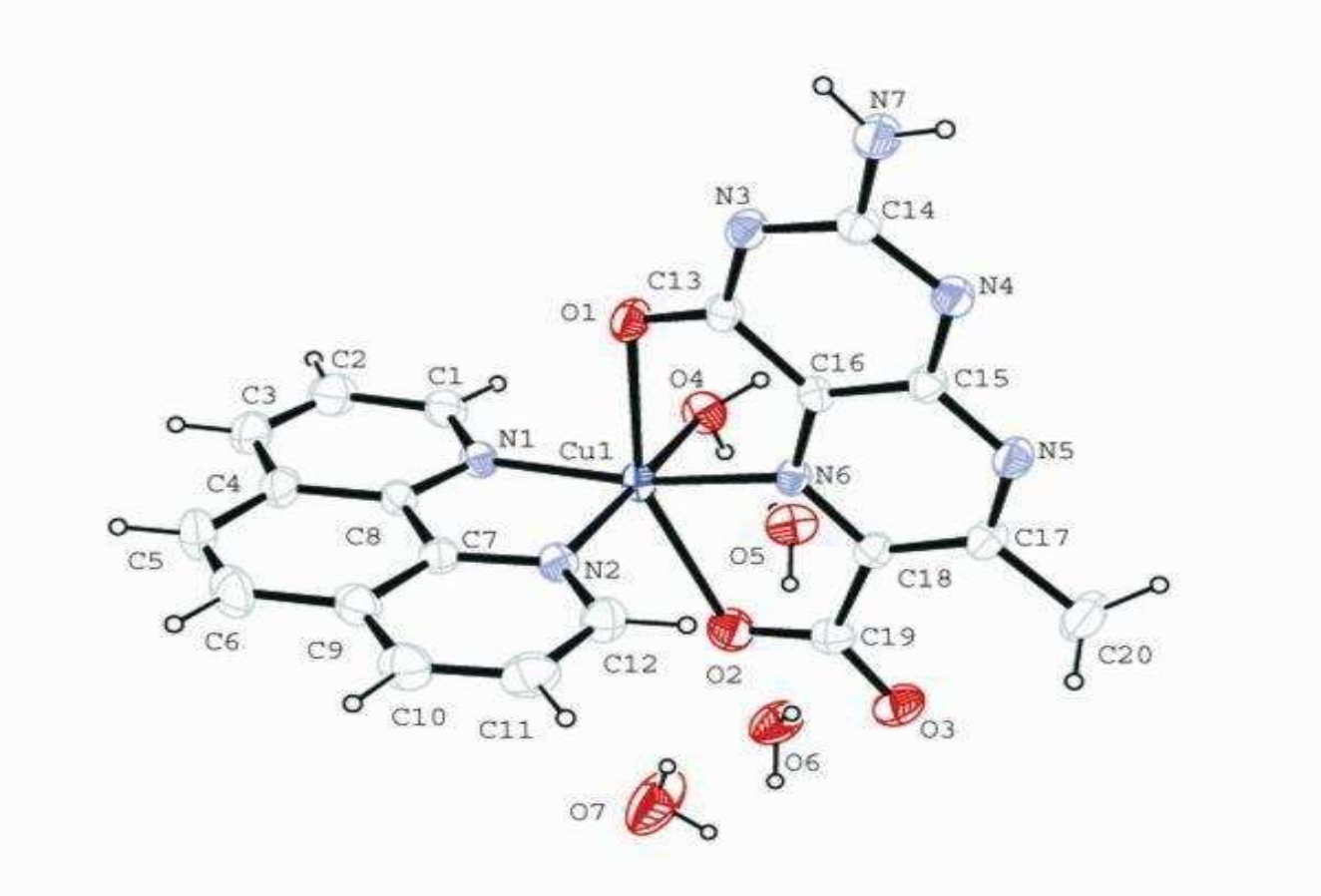

Figure II- 3. The molecular structure of **2**, with the displacement ellipsoids drawn at the 30% probability level. Few relevant bond lengths (Å) and angles (deg) are shown here : Cu1-N1=2.002(3), Cu1 – N2= 2.037(3), Cu1 – N6= 1.999(3), Cu1 – O1= 2.384(3), Cu1 – O2= 2.304(3), Cu1 – O4= 2.019(3), O1 – C13= 1.237(5), N7 – C14=1.327(5); O2 – Cu1 – O1=151.17(10), N6 – Cu1 – N1=165.66(13), O4 – Cu1 – N2=174.45(13), N6 –Cu1 – O1=76.47(10), N6 – Cu1- O2= 74.66(11)[17b].

Molecular structure of [Cu^{II}(L)(phen)(H_2O)]. $3H_2O$ (2). Figure II-3 shows a mononuclear Cu(II) centre in an axially elongated distorted octahedron, with two N atoms (N1 and N2) of the phen ligand, a pyrazine ring N atom (N6) of the pterin ligand and the aqua O atom (O4), forming the equatorial plane. The two pterin O atoms (O1 and O2) occupy the longer axial positions, with

the phenolate O1 forming the longest axial bond [2.384(3)Å]. In addition to the characteristic Jahn-Teller effect, another factor causing deviation from a regular octahedral geometry is that the pterin ligand forms two five-membered chelate rings with small bite angles [76.47(10) and $74.66(11)^0$]. In terms of the charge balance of this complex, the pterin ligand (**1**) acts as a binegative tridentate O,N,O - donor (Schemes II-1 and II-3). The phen ligand and pterin chelate ring are disposed almost orthogonally [dihedral angle = $85.97(3)^0$], thereby minimizing the steric repulsion. Of the three axes, the least deviation from linearity is observed along the O4-Cu1-N2 direction [$174.45(13)^0$]. The pyrazine ring N atom (N6) forms the shortest Cu1-N6 bond [1.999(3)Å] here and is located in the equatorial plane, maintaining parity with the earlier observations on related copper and cobalt complexs[17e,18c].The multiple bond character of the O1-C13 bond [1.237(4)Å] merits attention, as it throws light on the electron-shuffling ability of the pterin ring as well as its donor groups. According to Joule's hypothesis, electron-density is withdrawn from the pyrazine ring N5 by the pyrimidine ring C13 carbonyl group through mesomeric interaction.[22,23] Formation of the O1-Cu1 bond helps this electron migration towards the O1 atom, with possible participation of the electron- rich N7-C14[1.327(5)Å] bond in this process. This view is substantiated by similar observations on related Co(II), Ni(II) and Zn(II) complexes.[17a,17c-17e] Table II-I shows the crystal data of **2**, while its geometric parameters and hydrogen-bond geometry data are shown in Tables II-2 and II-3 respectively.

Table II-1. Crystal data of **2**

Chemical formula	$[Cu(C_8H_5N_5O_3)(C_{12}H_8N_2)(H_2O)]\cdot 3H_2O$
M_r	534.98
Crystal system, space group	Triclinic, $P\bar{1}$
Temperature (K)	273
a, *b*, *c* (Å)	8.5399 (17), 10.038 (2), 13.601 (3)
α, β, γ (°)	97.292 (3), 94.587 (3), 110.999 (3)
V (Å^3)	1069.8 (4)
Z	2
Radiation type	Mo *K*α
μ (mm^{-1})	1.08
Crystal size (mm)	0.20 × 0.05 × 0.03
Data collection	
Diffractometer	Bruker Kappa APEXII
Absorption correction	Multi-scan (*SADABS*; Bruker, 2001)
T_{min}, T_{max}	0.813, 0.968
No. of measured, independent and observed [$I > 2\sigma(I)$] reflections	8227, 4134, 3590

R_{int}	0.024
$(\sin \theta/\lambda)_{max}$ (Å^{-1})	0.617
Refinement	
$R[F^2 > 2\sigma(F^2)]$, $wR(F^2)$, S	0.051, 0.136, 1.15
No. of reflections	4134
No. of parameters	349
No. of restraints	10
H-atom treatment	H atoms treated by a mixture of independent and constrained refinement
$\Delta\rho_{max}$, $\Delta\rho_{min}$ (e Å^{-3})	0.66, −0.31

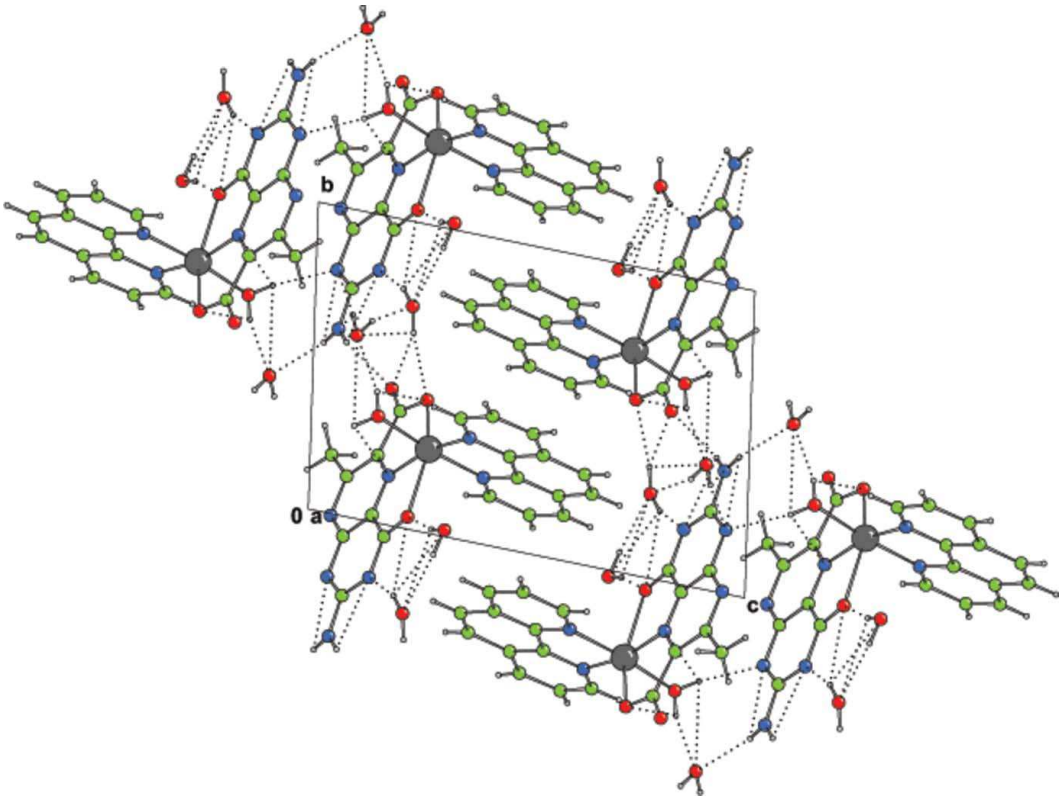

Figure II-4. The crystal packing diagram of the title compound, viewed along the a axis. Hydrogen bonds (dotted lines) assist the formation of a layer structure parallel to (001).

Table II-2. Geometric parameters (Å, °) of **2**

Cu1—O3	2.400 (7)	C15—C14	1.448 (13)
Cu1—N3	2.002 (7)	C15—C20	1.476 (14)
Cu1—N1	2.034 (8)	N6—H61	0.859
Cu1—O1	2.303 (7)	N6—H62	0.859
Cu1—N2	1.995 (8)	N6—C17	1.322 (13)

Cu1—O4	2.024 (7)	C9—C8	1.407 (13)
O3—C18	1.248 (11)	C8—C10	1.400 (16)
N3—C19	1.313 (12)	C8—C7	1.407 (16)
N3—C14	1.328 (12)	C4—C6	1.438 (15)
N1—C5	1.355 (12)	C4—C3	1.403 (16)
N1—C1	1.324 (12)	C12—H121	0.930
O1—C13	1.270 (12)	C12—C11	1.385 (14)
N2—C9	1.372 (12)	C1—H11	0.932
N2—C12	1.313 (12)	C1—C2	1.401 (15)
N4—C16	1.350 (12)	C10—H101	0.928
N4—C15	1.318 (13)	C10—C11	1.375 (17)
N7—C18	1.332 (13)	C20—H201	0.969
N7—C17	1.368 (12)	C20—H202	0.954
C16—C19	1.416 (11)	C20—H203	0.955
C16—N5	1.326 (12)	C6—H61	0.934
C19—C18	1.451 (13)	C6—C7	1.340 (18)
O2—C13	1.246 (12)	C3—H31	0.926

N5—C17	1.355 (12)	C3—C2	1.357 (17)
C13—C14	1.505 (14)	C7—H71	0.930
C5—C9	1.414 (13)	C2—H21	0.929
C5—C4	1.399 (13)	C11—H111	0.930
O3—Cu1—N3	76.4 (3)	H61—N6—C17	120.0
O3—Cu1—N1	91.0 (3)	H62—N6—C17	119.8
N3—Cu1—N1	93.9 (3)	C5—C9—N2	117.5 (8)
O3—Cu1—O1	151.3 (2)	C5—C9—C8	120.0 (9)
N3—Cu1—O1	75.0 (3)	N2—C9—C8	122.5 (9)
N1—Cu1—O1	89.8 (3)	N7—C17—N5	126.0 (9)
O3—Cu1—N2	89.6 (3)	N7—C17—N6	115.8 (8)
N3—Cu1—N2	165.4 (3)	N5—C17—N6	118.3 (9)
N1—Cu1—N2	82.2 (3)	C13—C14—C15	127.3 (9)
O1—Cu1—N2	118.9 (3)	C13—C14—N3	115.2 (8)
O3—Cu1—O4	92.9 (3)	C15—C14—N3	117.5 (9)
N3—Cu1—O4	90.7 (3)	C9—C8—C10	116.7 (10)
N1—Cu1—O4	174.6 (3)	C9—C8—C7	118.5 (10)

O1—Cu1—O4	88.7 (3)	C10—C8—C7	124.8 (10)
N2—Cu1—O4	94.0 (3)	C5—C4—C6	118.7 (10)
Cu1—O3—C18	106.3 (6)	C5—C4—C3	116.7 (10)
Cu1—N3—C19	116.8 (6)	C6—C4—C3	124.6 (10)
Cu1—N3—C14	121.1 (7)	N2—C12—H121	118.5
C19—N3—C14	122.1 (8)	N2—C12—C11	123.4 (10)
Cu1—N1—C5	111.8 (6)	H121—C12—C11	118.1
Cu1—N1—C1	130.0 (7)	N1—C1—H11	118.8
C5—N1—C1	118.2 (9)	N1—C1—C2	122.0 (10)
Cu1—O1—C13	112.3 (6)	H11—C1—C2	119.2
Cu1—N2—C9	111.8 (6)	C8—C10—H101	120.2
Cu1—N2—C12	129.7 (7)	C8—C10—C11	120.1 (9)
C9—N2—C12	118.2 (8)	H101—C10—C11	119.7
C16—N4—C15	120.8 (8)	C15—C20—H201	109.5
C18—N7—C17	118.6 (8)	C15—C20—H202	109.2
N4—C16—C19	118.4 (8)	H201—C20—H202	109.1
N4—C16—N5	120.6 (8)	C15—C20—H203	109.4

C19—C16—N5	121.0 (8)	H201—C20—H203	109.1
C16—C19—N3	120.7 (8)	H202—C20—H203	110.4
C16—C19—C18	118.8 (8)	C4—C6—H61	120.1
N3—C19—C18	120.5 (8)	C4—C6—C7	120.2 (10)
C19—C18—N7	118.3 (9)	H61—C6—C7	119.7
C19—C18—O3	119.8 (9)	C4—C3—H31	120.5
N7—C18—O3	121.9 (8)	C4—C3—C2	119.7 (10)
C16—N5—C17	117.2 (8)	H31—C3—C2	119.7
O1—C13—O2	124.1 (10)	C8—C7—C6	122.5 (10)
O1—C13—C14	116.1 (9)	C8—C7—H71	118.6
O2—C13—C14	119.7 (9)	C6—C7—H71	118.9
N1—C5—C9	116.4 (8)	C1—C2—C3	119.9 (10)
N1—C5—C4	123.5 (9)	C1—C2—H21	120.0
C9—C5—C4	120.1 (9)	C3—C2—H21	120.1
N4—C15—C14	120.4 (8)	C12—C11—C10	119.0 (10)
N4—C15—C20	117.9 (9)	C12—C11—H111	120.4
C14—C15—C20	121.7 (10)	C10—C11—H111	120.6

H61—N6—H62	120.2		

Supramolecular features. In the crystal, intermolecular N—H----O, O—H----N and O—H----O hydrogen bonds (Table II-3) link the complex molecules and lattice water molecules into a layer parallel to (001) (Figure II- 4). Intermolecular weak C—H----O hydrogen bonds and C—H----π interactions are also observed in the crystal. In addition, π-π stacking between nearly parallel pterin ring systems of adjacent molecules occurs in the crystal structure, the centroid–centroid distance being 3.352 (2) A ° (Figure II- 5). Again, the nearly parallel phen rings of adjacent molecules also display π-π stacking interactions with centroids distances of 3.546 (3), 3.706 (3) and 3.744 (3) A ° . These intermolecular interactions link the molecules into a three-dimensional supramolecular architecture.

Table II-3. Hydrogen-bond geometry (Å, °) of **2**, *Cg* is the centroid of the N3/N4/C13–C16 ring.

D*—H···*A	***D*—H**	**H···*A***	***D*···*A***	***D*—H···*A***
O4—H4*C*···O5	0.82 (3)	1.92 (3)	2.722 (4)	169 (5)
O4—H4*D*···N4^{i}	0.81 (3)	2.26 (3)	3.038 (4)	161 (5)
O5—H5*C*···O6	0.82 (3)	1.96 (4)	2.748 (5)	162 (4)
O5—H5*D*···N4^{ii}	0.82 (5)	2.07 (5)	2.891 (5)	176 (3)

D*—H···*A	***D*—H**	**H···*A***	***D*···*A***	***D*—H···*A***
O6—H6*C*···O2	0.82 (3)	2.23 (3)	2.921 (4)	141 (5)
O6—H6*C*···O3	0.82 (3)	2.25 (4)	3.029 (4)	158 (5)
O7—H7*C*···O6	0.82 (2)	2.24 (3)	2.965 (6)	148 (5)
O7—H7*D*···O1^{iii}	0.81 (5)	2.16 (4)	2.943 (6)	162 (5)
N7—H7*E*···O5^{i}	0.85 (5)	2.17 (4)	2.998 (6)	162 (4)
N7—H7*F*···O3^{iv}	0.86 (4)	2.14 (5)	2.908 (5)	148 (4)
C1—H1···O3^{v}	0.93	2.47	3.175 (6)	133
C10—H10···O1^{vi}	0.93	2.54	3.406 (5)	155
C12—H12···O7^{vii}	0.93	2.57	3.343 (7)	140
C6—H6···*Cg*^{vi}	0.93	2.82	3.740 (5)	173

Symmetry codes: (i) -*x*+2, -*y*+2, -*z*+2; (ii) *x*, *y*-1, *z*; (iii) *x*-1, *y*-1, *z*; (iv) *x*+1, *y*+1, *z*; (v) *x*+1, *y*, *z*; (vi) -*x*+2, -*y*+2, -*z*+1; (vii) *x*,*y*+1, *z*.

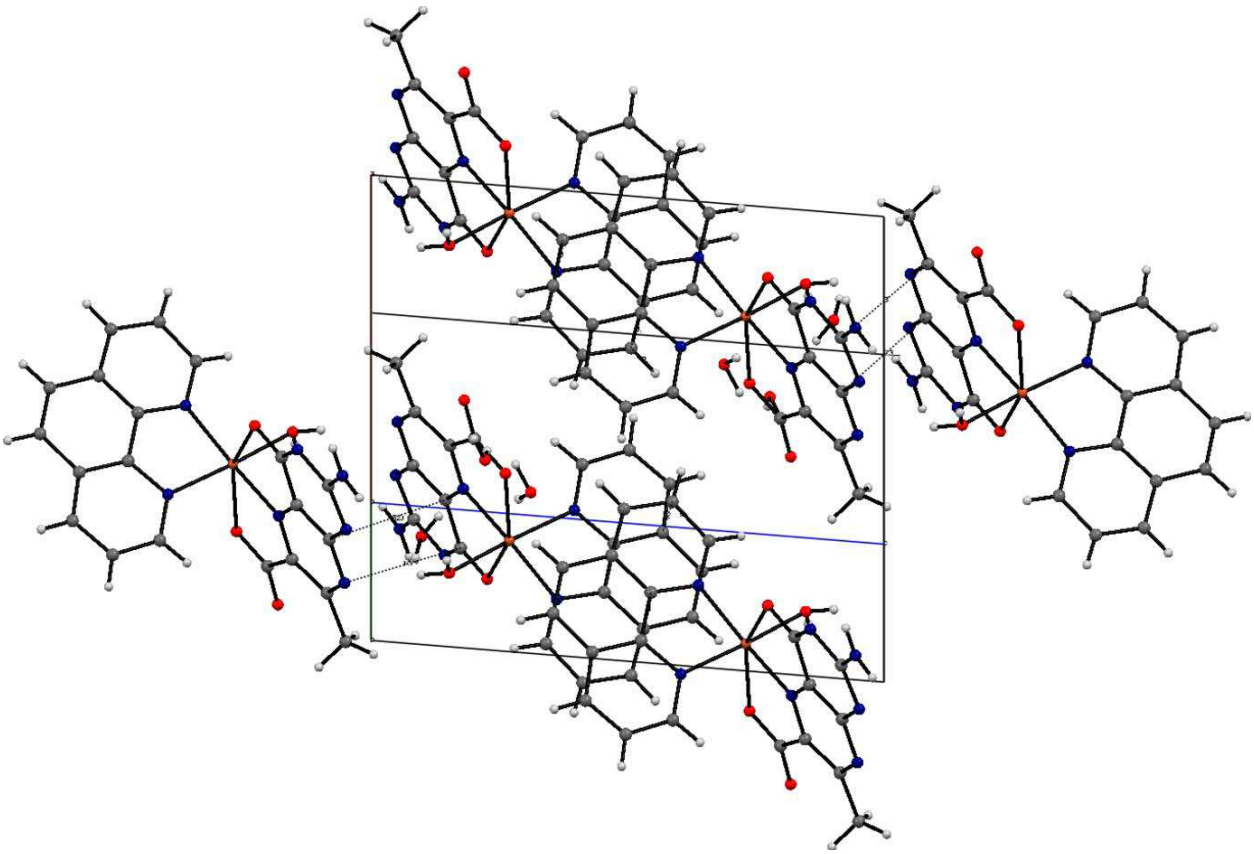

Figure II-5. A molecular packing diagram highlighting π-π stacking interactions between neighbouring phen–phen and pterin–pterin rings.

Table II – 4. Selected optimized geometric parameters (Å, °) of **3**[155-160] and their comparison with the related x-ray structural data of **2**.

Bonds (Å)	DFT optimized data of **3** (Gaussian 09)	x-ray structural data of **2** (Table II-2)[17b]	MM2 optimized (CHEM 3D) data of **3**
Cu(15) – N(9)	2.3782	2.002(3)	2.378
Cu(16) – N(14)	2.3881	2.037(3)	2.388
Cu(15) – O(45)	1.9871	2.384(3)	1.987

Cu(15) – O(48)	1.9469	2.304(3)	1.947
Cu(15) – O(49)	1.9138	2.019(3)	1.914
Cu(15) – O(50)	1.922	2.019(3)	1.922
Cu(15) – N(42)	1.8902	1.999(3)	1.890
Cu(16) – N(26)	1.8959	1.999(3)	1.896
Cu(16) – O(51)	1.9314	2.019(3)	1.931
Cu(16) – O(52)	1.9144	2.019(3)	1.914
Cu(16) – O(32)	1.9501	2.384(3)	1.950
Cu(16) – O(29)	2.0335	2.304(3)	2.033

Bond angles (°)	DFT optimized data of **3** (Gaussian 09)	x-ray structural data of **2** (Table II-2)[17b]	MM2 optimized (CHEM 3D) data of **3**
O(45) – Cu(15) – O(48)	168.1866	151.17(10)	168.187
N(9) – Cu(15) – N(42)	177.3987	165.66(13)	177.399
N(9) – Cu(15) – O(45)	93.6388	89.79(11)	93.639
N(9) – Cu(15) – O(48)	98.157	118.84(12)	98.157
N(9) – Cu(15) – O(50)	90.2632	82.20(13)	90.263
N(9) – Cu(15) – O(49)	92.5509	93.79(13)	92.551
N(42) – Cu(15) – O(45)	83.828	76.45(11)	83.828
N(42) – Cu(15) – O(48)	84.37	74.74(11)	84.370
N(42) – Cu(15) – O(49)	86.8199	91.01(12)	86.820
N(42) – Cu(15) – O(50)	90.3314	93.79(13)	90.331

O(45) – Cu(15) – O(50)	90.0711	90.74(12)	90.071
O(45) – Cu(15) – O(49)	88.9062	93.07(12)	88.906
O(50) – Cu(15) – O(48)	90.5147	88.62(12)	90.515
O(49) – Cu(15) – O(48)	89.924	89.98(12)	89.924
O(49)-Cu(15)-O(50)	177.0611	174.45(13)	177.061
N(26) – Cu(16) – N(14)	173.5472	165.66(13)	173.547
O(29) – Cu(16) – O(32)	166.3806	151.17(10)	166.381
N(14) - Cu(16) – O(29)	103.4795	118.84(12)	103.479
N(14) - Cu(16) – O(51)	89.9923	89.79(11)	89.992
N(14) - Cu(16) – O(52)	91.2396	93.79(13)	91.240
N(14) - Cu(16) – O(32)	90.1385	82.20(13)	90.138
N(26) – Cu(16) – O(29)	82.9732	76.45(11)	82.973
N(26) – Cu(16) – O(32)	83.4088	74.74(11)	83.409
N(26) – Cu(16) – O(51)	90.01	91.01(12)	90.010
N(26) – Cu(16) – O(52)	88.7801	93.79(13)	88.780
O(29) – Cu(16) – O(51)	90.3224	88.62(12)	90.322
O(29) – Cu(16) – O(52)	89.2679	89.98(12)	89.268
O(51) – Cu(16) – O(32)	89.8661	89.79(11)	89.866
O(52) – Cu(16) – O(32)	90.257	93.79(13)	90.257
O(51)-Cu(16)-O(52)	178.7621	174.45(13)	178.762

DFT optimized molecular structure of 3

Scheme II-5(a) shows the relevant optimized molecular structure of **3**[155-159]. It takes into account the 7, 8-dihydro form of the pterin ring (L'^{2-}, Scheme II-4) as well as the bridging 'phen' ligand; it is consistent with its microanalytical, ESIMS, physico-chemical (cyclic voltammetry) and spectroscopic (UV-VIS, IR, fluorescence and ^{1}H NMR) data. In short an effective frame work is obtained for further discussion (vide later). Here **3** consists of two octahedrally coordinated Cu(I) centres linked by a bridging 'phen' ligand; the latter is disposed almost orthogonally to the two pterin rings for minimizing the steric repulsions and it is puckered to a certain extent. Along with tridentate ONO coordination from the pterin ligand, the two aquo ligands complete the coordination octahedron around each copper (I) atom. The MM2 calculations (CHEM 3D model) provide with an almost identical optimized structure.[160] Table II-4 shows a few selected optimized geometric parameters (Å, °) of **3** obtained by either DFT (Gaussian 09) method or MM2 calculations (Chem 3D); they are compared with the x-ray structural data of **2**.[17b] The tally of computed/optimized data with the x-ray structural data is reasonable, in view of the fact that **3** possesses two Cu(I) centres linked by a μ-phen group and two 7, 8-dihydro pterin ligands instead of a mononuclear Cu(II) centre of **2** with aromatic/oxidized pterin.

Chemical composition and mass spectrometry. For all the compounds mentioned in the experimental section (**1, 2** and **3**) as well as the green compound recovered from the methanolic reaction medium involving **3** and bromobenzene, identified here as **2** [Scheme II- 8(b)], satisfactory elemental analysis data and electrospray ionization mass spectra (ESIMS) have been obtained. For **1** a peak at m/z 222 (rel. inten.15%) corresponds to the dehydrated species $[M - 1.5H_2O + H]^+$ where $M(C_8H_7N_5O_3.\ 1.5H_2O)$ is the relevant molecular formula; the associated

isotope pattern could be calculated.[21,24] For **2** the intact molecular ion peak ($[M + H]^+$) is observed at m/z 536.4 (rel. inten. 40%), where M = $CuC_{20}H_{13}N_7O_3 . 4H_2O$; the base peak at m/z 459.2 represents the corresponding dehydrated species $[M – 4H_2O – 3H]^+$ and its isotope distribution pattern

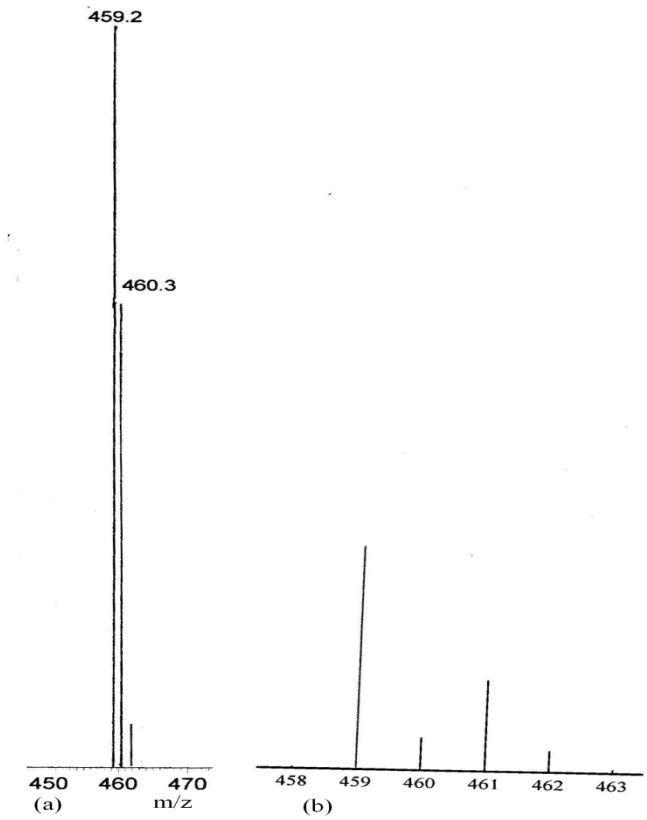

Figure II-6. (a) ESIMS data of **2,** m/z = 459.2; (b) the calculated isotope pattern for the base peak at m/z = 459.2 corresponding to the fragment $[M – 4H_2O – 3H^+]^+$, where M is the molecular formula of **2**.

---

could be simulated (Figure II-6). For the green compound recovered from the reaction sequence summarized in Scheme II-8(b), the base peak at m/z 463.36 could be assigned to the desolvated

molecular ion [M – $4H_2O$]$^+$ where M is identified to be **2**, i.e., M= $CuC_{20}H_{13}N_7O_3$. $4H_2O$; the relevant simulated isotope pattern is shown in Figure II-7. Finally, the ESIMS

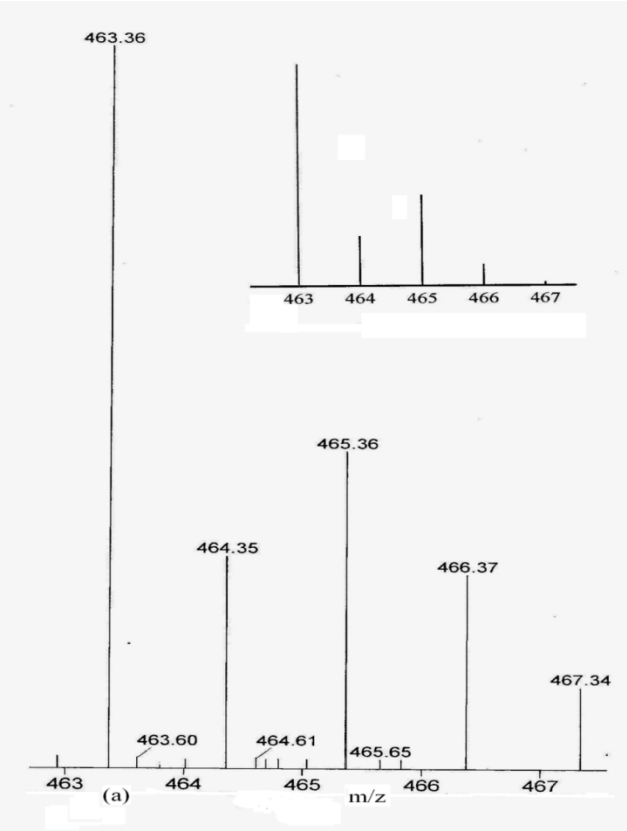

Figure II-7. (a) ESIMS data (m/z = 463.36) of **2** recovered from a reaction mixture, as indicated in Scheme II-8(b); (b) the corresponding calculated isotope pattern for the fragment [M – $4H_2O$]$^+$, where M is the molecular formula of **2**.

---

data [Figure II- 8(a)] are able to substantiate the composition of **3**, that is, its binuclear formulation. The peak at m/z 808.9 (rel. inten. 20%) is assigned to the fragment [M – $5H_2O$ – $5H$]$^+$ where M is **3** (M= $Na_2Cu_2C_{28}H_{22}N_{12}O_6$. $6H_2O$); the loss of five H atoms is justified for a fragment ion peak.[21] The peak at m/z 705.0 (rel. inten. 32%) corresponds to the fragment [M – $6H_2O$ – $2CO_2$ – $2H$]$^+$. The isotope distribution patterns of both these peaks could be simulated

[Figure II-8(b), (c)], verifying the overall stability of the parent binuclear species (**3** , Scheme II-5) as well as its chemical composition.

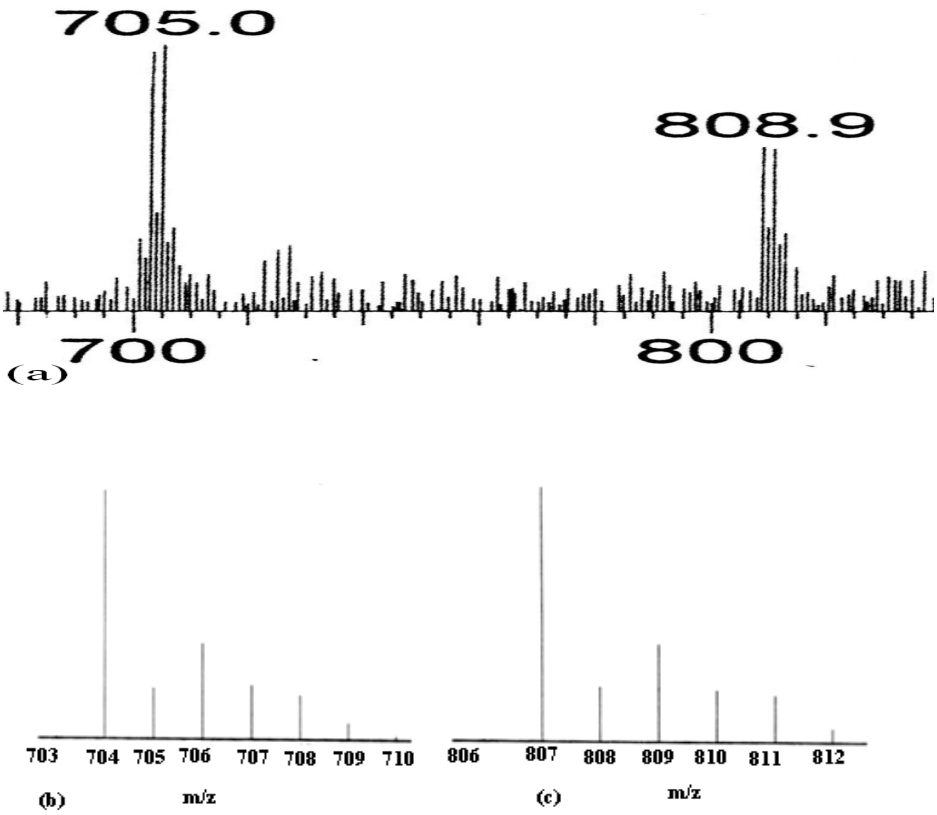

Figure II-8. (a) ESIMS data (m/z = 705.0 and 808.9) of **3**; the corresponding calculated isotope patterns are shown in (b) and (c).

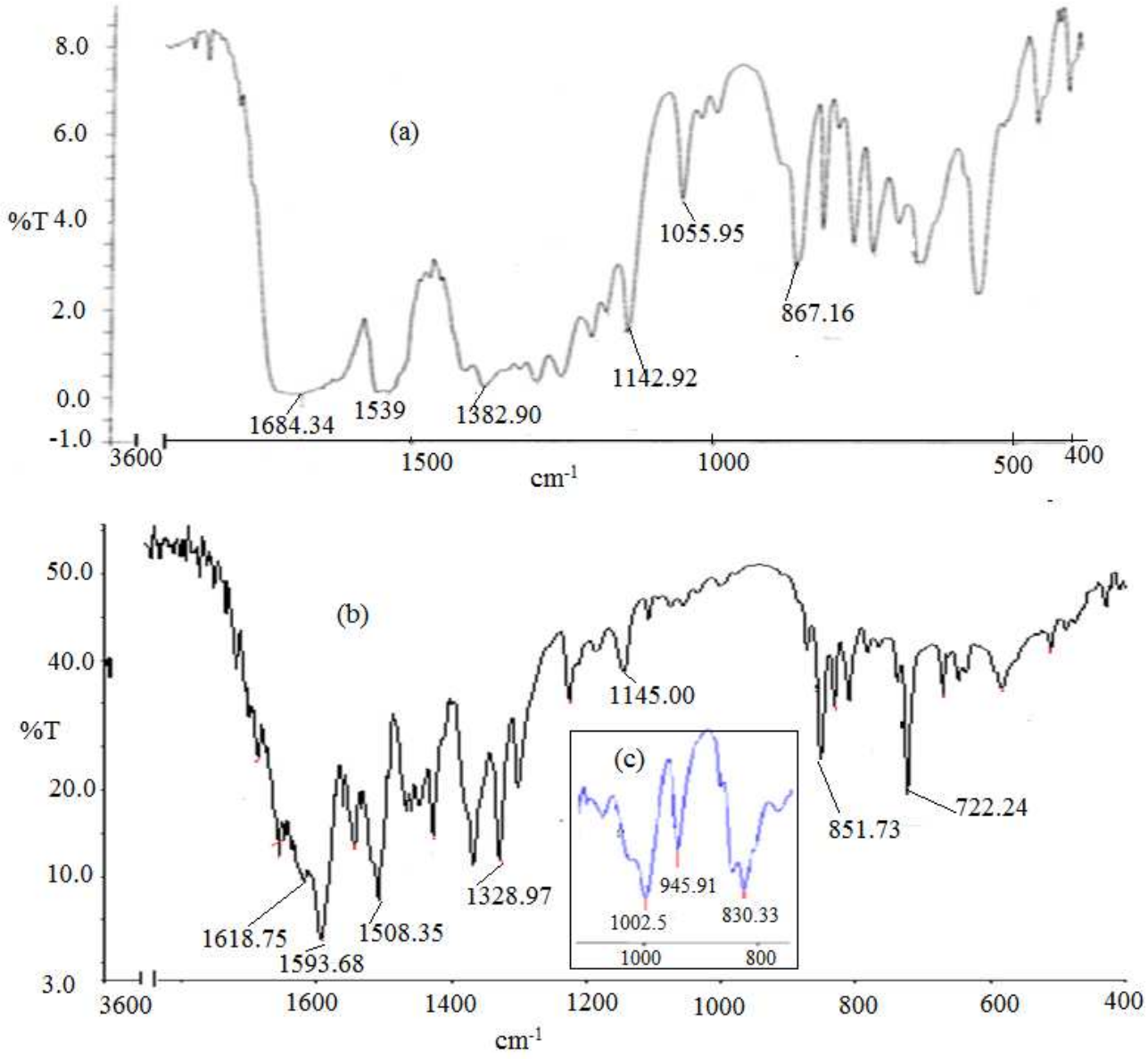

Figure II-9. IR spectra (KBr) (characteristic region) of **1** (a), **2** (b) with that of **3**(c) being included for visualizing the $NaBH_4$ reduction of **2** (Scheme II-4, II-8); Figures II-10 and II-11 show their complete spectra (3600-400 cm^{-1}).

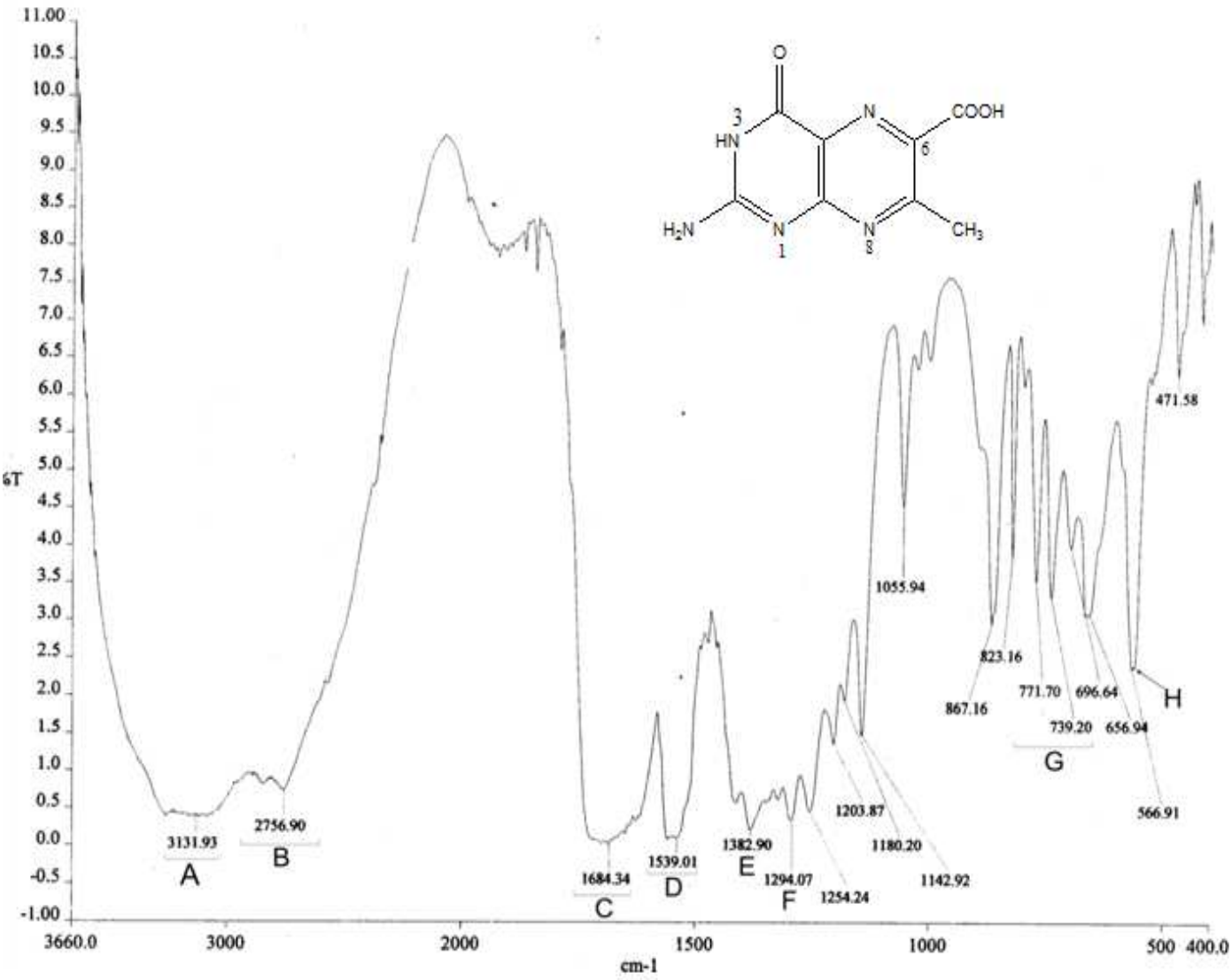

Figure II-10. IR spectrum (KBr) of **1**

A: the broad band over the region 3250-3050 cm^{-1} due to the ν(OH) and ν(NH) stretching vibrations of the hydrogen bonded H_2O, - COOH(6), NH(3) and NH_2(2) groups , Scheme III-1;

B: the ν(CH) stretching vibrations of the CH_3(7) group are observed at 2851 cm^{-1} and 2757 cm^{-1} respectively;

C: an intense broad band centred at 1684 cm^{-1} and spread over the region 1718-1636 cm^{-1} is due to the ν(C=O) modes of the C=O(4) and COOH(6) groups, (Scheme III-1); the N-H bending vibrations at the NH_2(2) group are occluded under this band;

D: the ν(C=C) and ν(C=N) modes at the pterin ring appears around 1560-1539 cm^{-1};

E&F: the δ(O-H) and ν(C-O) + δ(O-H) modes of the COOH(6) group appear at 1382 cm^{-1} and 1294 cm^{-1} respectively;

G: different types of skeletal bending vibrations of the pterin ring appear over the region 860-650 cm^{-1};

H: rocking vibrations of the NH_2(2) group appears around 567 cm^{-1}.

IR Spectrscopy. The comparative IR spectra (KBr pellets) of **1** and **2** are shown in Figure II-9. For **1** [Figure II- 10] an intense broad band extending over the region 3250 – 3050 cm^{-1} along with a shoulder at 3367 cm^{-1} corresponds to the ν(OH) and ν(NH) stretching vibrations of the hydrogen bonded lattice water molecules, the COOH(6), NH(3) and NH_2(2) groups. The ν(CH) stretching vibrations of the CH_3(7) group appear at 2851 and 2757 cm^{-1} respectively.[21] Another intense broad band centred around 1684 cm^{-1} and spread over the region 1718 to 1636 cm^{-1}, characterizes the ν(C=O) modes of the C=O(4) group as well as that of the COOH(6) group. Some of the ν(C=C) and ν(C=N) modes of the pterin ring could be identified around 1560-1539 cm^{-1}.[25-28] Two other broad bands at 1383 cm^{-1} and 1294 cm^{-1} characterize the δ(O-H) and ν(C-O) + δ(O-H) modes of the COOH(6) group.[21] Most of the above-mentioned broad bands of **1** undergo considerable modification through complex formation with the Cu(II) ion, as evident from the IR spectrum of **2** [Figure II- 11(a)] (Schemes II-1to II-3). The ν(OH) and ν(NH) modes of the hydrogen bonded intra- and extra spheric water molecules and the NH_2(2) group appear at 3401 cm^{-1} and 3336 cm^{-1} respectively. The ν(CH) modes of the phen moiety appear at 3158 cm^{-1}

and 3077 cm^{-1} respectively. The ν_{as} and ν_s $C(....O)_2$ stretching vibrations of the carboxylate group(6) appear at 1594 cm^{-1} and 1368 cm^{-1} respectively .[21] The ν(C=O) mode of the coordinated C=O(4) group (Schemes II- 1, II-3) could be assigned at 1619 cm^{-1}; this is consistent with the multiple bond character of the O1-C13 bond with a bond length of 1.237(4)Å (Figure II-3.).[17b] Several sharp peaks over the region 1545-1426 cm^{-1} as well as the one at 1329 cm^{-1} correspond to the ν(C = C) and ν(C = N) vibrations of the pterin ring.[25-28] The C-H out- of- plane bending vibrations of the phen moiety appear at 852 cm^{-1} and 722 cm^{-1} respectively; for 1, 10-phenanthroline monohydrate such vibration appear at 850 cm^{-1} and 740 cm^{-1} respectively.[21] Evidently, the IR spectral data of the different functional groups of **2** are consistent with its chemical composition and the x-ray structural data.[17b] IR spectrum of **3** [Figure II-11(b)] (Schemes II-4 to II-6) possesses an intense broad band centered around 3357 cm^{-1} associated with shoulders over the region 3461-3052 cm^{-1}, representing the above-mentioned ν(OH), ν(NH), ν(CH) modes. The ν_{as} and ν_s $C(.....O)_2$ stretching vibrations of the carboxylate group(6)(Scheme II-1) are observed at 1606 cm^{-1} and 1369 cm^{-1} respectively. The ν(C = O) mode of the C = O (4) group appears at 1632 cm^{-1}. The characteristic vibrations of the pterin ring (over the region 1518-1428 cm^{-1}) and the phen moiety (at 830 cm^{-1} and 723 cm^{-1}) are observed as well. An interesting feature of this spectrum [Figure II-9(c)] is the appearance of two new sharp peaks at 1002 cm^{-1} and 946 cm^{-1} assignable to the N – H (8) and C – H (7) out-of-plane bending vibrations respectively, of the 7,8-dihydro form of the pterin moiety of **3** (Schemes II-4 and II-6).[29-30] This view is supported by the ^1H NMR spectrum of **3** (vide later).

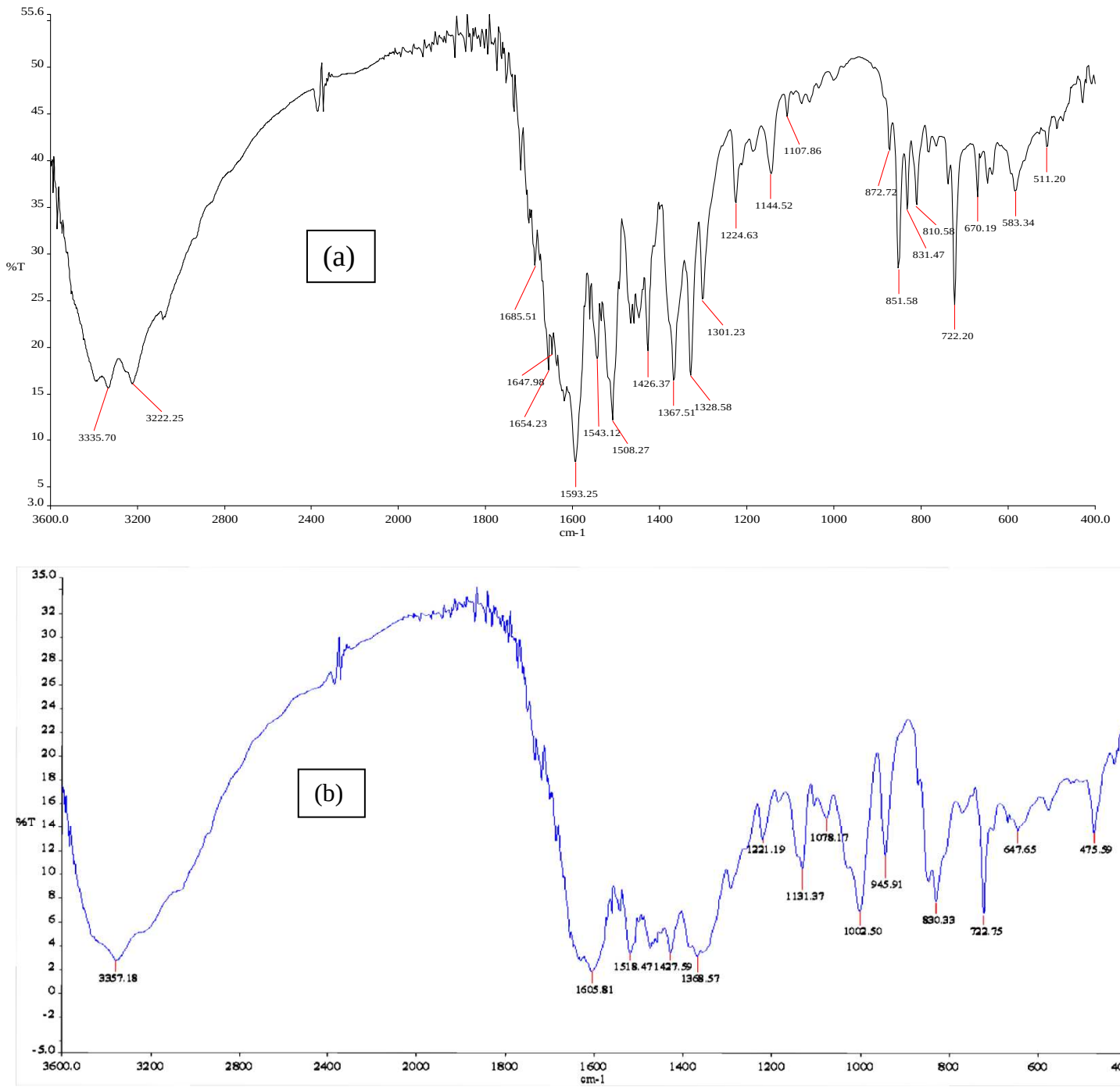

Figure II-11. IR spectra (KBr) of **2**(a), Scheme II-3 and **3**(b), Scheme II-4 to II-6.

Electronic spectroscopy. The electronic spectral data of the present copper complexes are presented in Table II- 5. For the green coloured complex **2**, the prominent band at 375 nm could

be assigned to a LMCT band. Its other absorption bands in the longer wavelength region (900 – 1100nm), possess much higher log ε values as compared to the usual ligand field(LF) transitions of the Cu(II) ion ; such high intensities could not be ascribed to even intensity stealing from the distant 375 nm band .[31] A closer look at the frontier MO diagram of **2** (Figure II-27) reveals that the phen and pterin ligand residues make major contributions to the SOMO, LUMO and LUMO+1 levels and there is a small band gap (0.22ev) between the last two levels conferring unique redox property.[64 – 66] The large log ε values (2.05 – 1.97) of the above longer wavelength bands (Table II-5), may be ascribed to MLCT transitions from occupied metal-centred orbitals (e.g., t_{2g}, e_g*) to vacant low lying ligand-centred orbitals (e.g., π* orbitals of pterin and phen). Such transitions are quite likely for **2** , a d^9 system with three electrons in the e_g* level (Scheme II-9). A Cu(II)-pteridine-phen mixed ligand complex possessing such a large logε value (2.21) at 705 nm has been reported earlier by Burgmayer and coworkers.[26] For the blue aqueous mother liquor (Table II-5), an intraligand π→π* transition and a LMCT transition are observed at 284 nm and 360 nm respectively; the broad band at 610 nm (ε = 51.56) may be assigned to a LF transition with intensity stealing.[31]

Electronic spectral data of **3** are characterized by more numerous bands of higher intensity as compared to those of **2** (Table II-5) and this observation may be traced to the following factors:

(i) **2** is a mononuclear Cu(II) (d^9) species (Scheme II-3), whereas **3** is a binuclear Cu(I) (d^{10}) species (Scheme II- 5) of lower symmetry, with attendant additional splitting of energy levels;

(ii) there is possibility of additional MLCT transitions of the type Cu(I) (d^{10}) → phen in **3** as well as increased electronic circulation in its [Cu(I) (phen)Cu(I)] core.[32]

Besides this, the frontier orbitals (Figure II-27) of **3** are also composed of mainly pterin and phen orbitals, with a small band gap (0.5 eV) between the HOMO-1 and HOMO-2 levels, thereby retaining the unique redox property.[64 -66]

Further verification of such assignments of MLCT transitions is provided by the corresponding Zn(II) complex (chapter VI)[17a], showing an intense MLCT broad band (logε = 4.086) at 733 nm which is responsible for its light brown color.

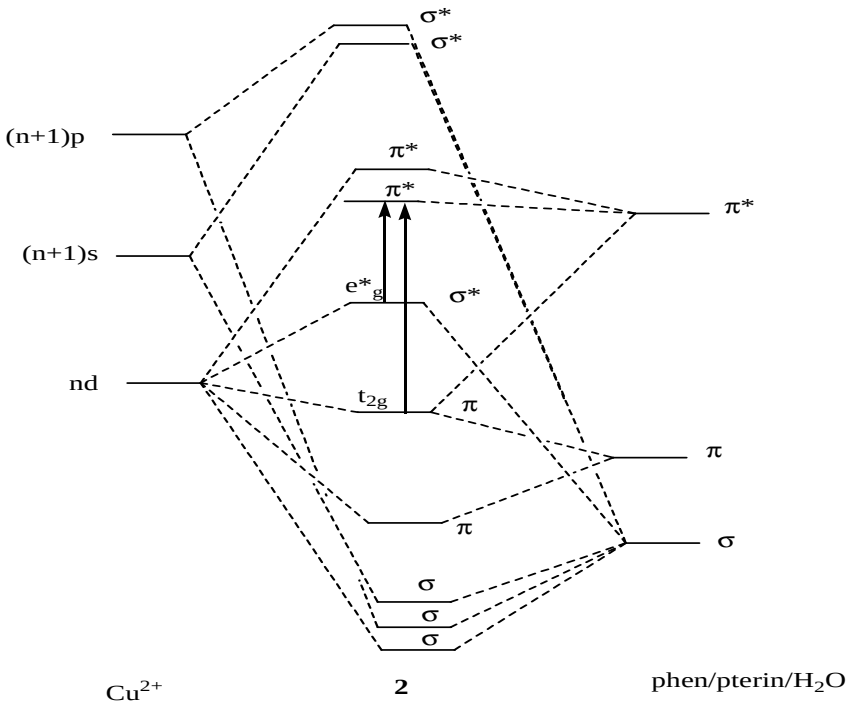

Scheme II-9 Simplified MO diagram for **2** indicating the possible metal-to-ligand charge transfer (MLCT) transition when both the e_g* and t_{2g} are nearly occupied and the ligands have empty π* orbitals; the metal-centred MOs of the former type are fully occupied for d^{10} ions like Cu(I) and Zn(II).[32]**.**

Table II-5. Electronic spectral data of **2, 3** and a related system.

Sl.No.	Compound (solvent)	λ_{max} nm (log ε)
1.	**2**(CH_3OH)	375(3.65), 905(2.05), 943(2.04),1015sh(1.97),1051br(1.98)
2.	Blue mother liquor(H_2O) *	284 (2.84), 360(2.26), 610br(1.71)
3.	**3**(CH_3OH)	360(3.84),366(3.82),830br(2.27),856sh(2.26),916sh(2.22),1034br(2.04), 1054sh(2.03),1071br(2.02)

*This mother liquor[Figure II-1(a)] refers to the synthesis of **2** by method A as described in reference 17b.

Fluorescence emission spectra. The fluorescence emission spectra of **2** , **3** and the aforesaid blue mother liquor are shown in Figure II-13 ; their emission maxima appear at 445 nm,442 nm and 456 nm respectively. Such emission maximum of the pterin ligand (**1**) (in aqueous NaOH solution) appears at 449 nm (Figure II-12). Fluorescence data constitute an important property of pterin compounds, e.g., such data provided with the initial evidence about the pterin component of the molybdenum cofactor.[33 - 34]

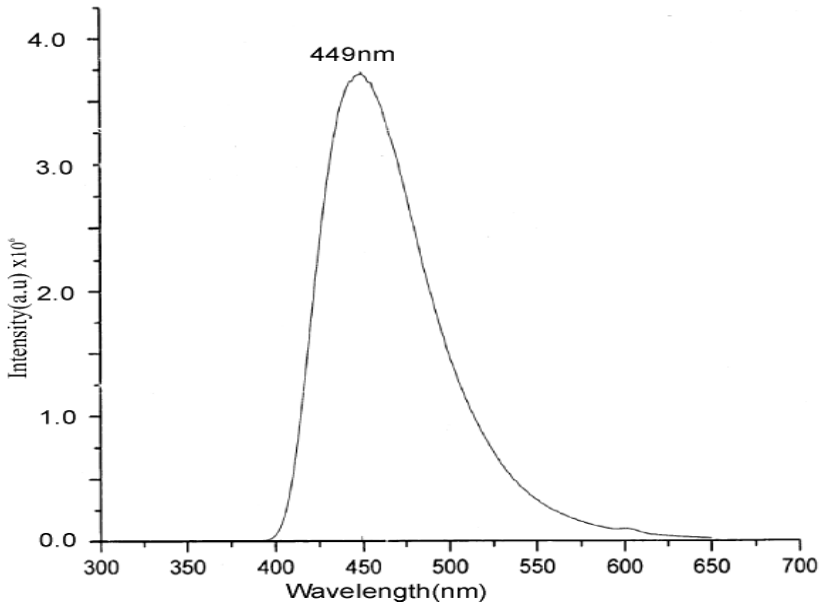

Figure II-12. Fluorescence emission spectrum of the pterin ligand (**1**) in aqueous NaOH solution.

The pH dependence of fluorescence property is also interesting, e.g., no fluorescence is observed for the protonated form of biopterin but the anion is strongly fluorescent.[35] Most organic fluorescent molecules contain conjugated system of double bonds with extended π-orbitals in a planar cyclic/rigid structure and not many loosely coupled substituents through which the vibronic energy can dissipate.[36] The common fluorophores include aromatic / heteroaromatic rings as well as functional groups like C = C, C = O , C =N, etc., while fluorochromes (usually electron donors) like – OH, - NH_2, etc., enhance the transition probability or fluorescence intensity. The fluorescence property of **1**, **2** and the blue mother liquor may be correlated with the aromatic / oxidized nature of the associated pterin ring. The enhanced fluorescence intensity of **3** (Figure II-13) which is obtained by the $NaBH_4$ reduction of **2** in CH_3OH, may be understood in the light of greater electronic circulation in its bridging unit [Cu(I) (phen) Cu (I)] (Scheme II-5) involving the Cu(I)(d^{10}) → phen type CT transition.[32]

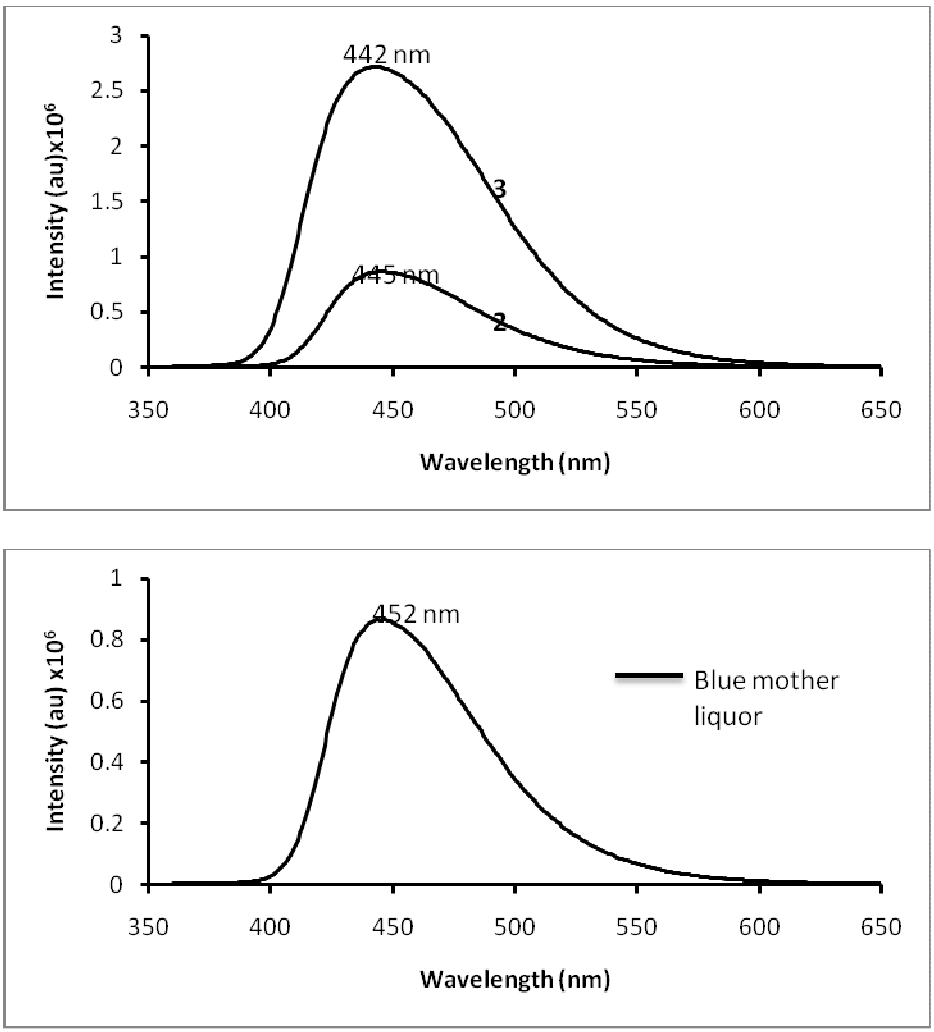

Figure II-13. Fluorescence emission spectra of **2** (CH_3OH, 1.4 x 10^{-4} M), **3** (CH_3OH, 1.4 x 10^{-4} M) and the blue aqueous mother liquor from which **2** was isolated (3.4 x 10^{-3}M).

EPR spectroscopy and magnetic susceptibility of 2. The EPR spectrum (DMSO, 77K) of **2** is shown in Figure II-14, which indicates axial symmetry.[37] This is consistent with its elongated distorted octahedral coordination geometry around the Cu(II) ion (Figure II-3).[17b] In a tetragonally elongated octahedron, the energy of the dz^2 orbital will be lower than that of the dx^2-

y^2 orbital and the unpaired electron of this d^9 system will be located in the latter orbital. For this case, theoretical arguments indicate $g_{\parallel} > g_{\perp} > 2$ and the relevant EPR parameters are assigned in Figure II-14.[38] According to magnetic susceptibility measurement data (298K), **2** exhibits a μ_{eff} value of 1.32 B.M. It is lower than the expected spin-only value (μ_s) of 1.73 B.M. This lowering of μ_{eff} value is possibly due to superexchange interaction between two complex molecules sharing each unit cell, as par the relevant crystal packing diagram of **2** (Figure II-5); the corresponding molecular packing diagram (Figure II-5) highlights the π-π stacking interactions between neighbouring phen-phen and pterin-pterin rings.[17b]

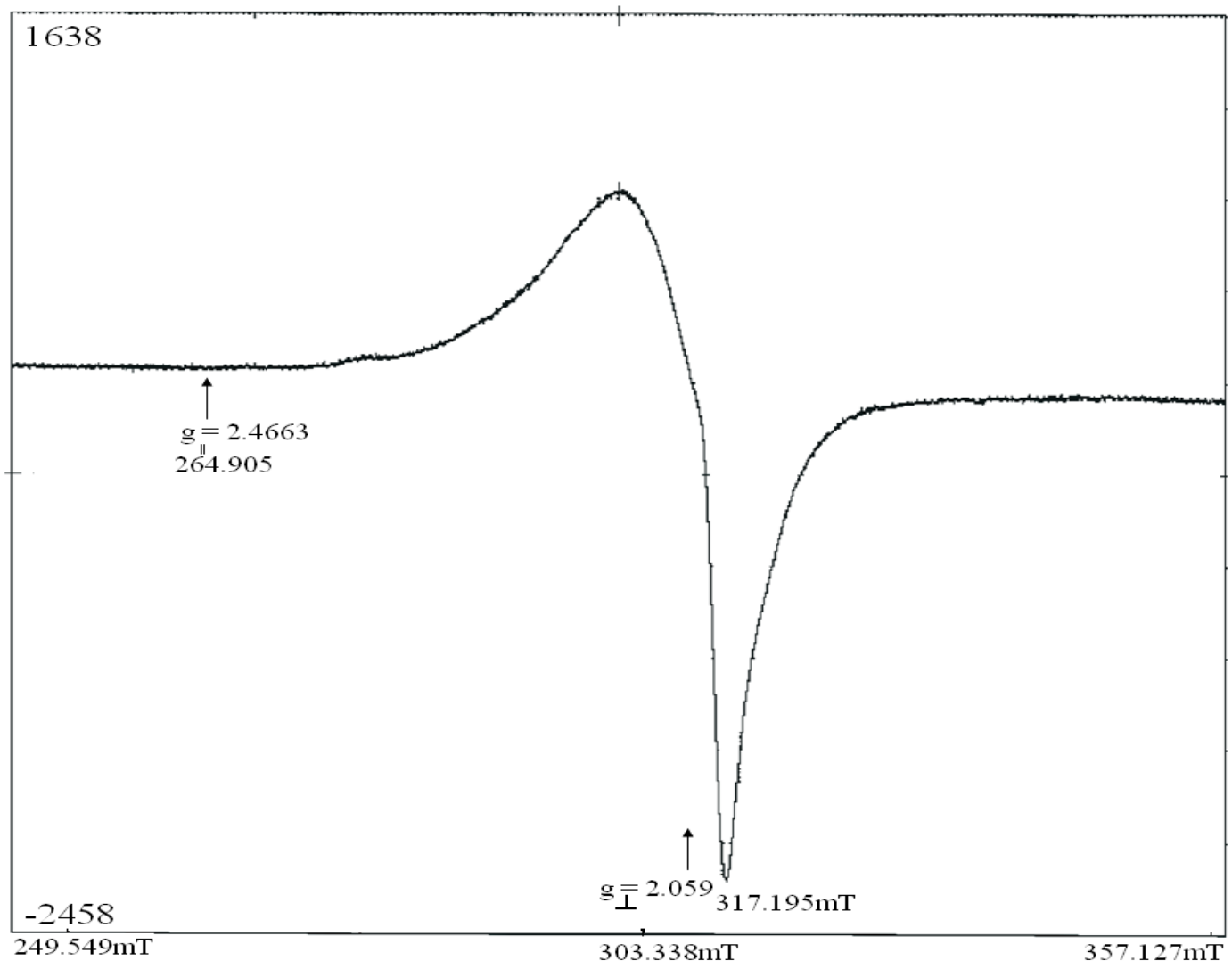

Figure II-14. X-band EPR spectrum of **2** in DMSO at 77K with a probe frequency of 9144.756 MHz and a field centre of 303.338 mT.

---

^{1}H NMR spectroscopy of 1 and 3. The ^{1}H NMR spectrum of **3** [Scheme II-5, II-5(a)] in DMSO-d_6 is shown in Figure II-15, with the NH(8) and CH(7) proton signals (Scheme II-4) being depicted on an expanded scale, which appear at δ 6.81 (w,br) and δ 8.32 (s,s) respectively; such signals are absent in case of **1** in NaOD/D_2O [L^{2-} in Scheme II-1, Figure II-16(a)]. These

two new signals for **3** result from the transfer of reducing equivalents from $NaBH_4$ to the double bond at the 7,8-position of the L^{2-} residue (Scheme II-1) of **2** (Scheme II-3, Figure II-3)(vide the experimental section for the synthesis of **3**; Scheme II-6):

$$L^{2-}\text{in } \mathbf{2} \text{ (Scheme II-3)} \xrightarrow[CH_3OH \text{ or } H_2O]{NaBH_4} L'^{2-}\text{in } \mathbf{3} \text{ (Schemes II- 4 and II- 5).}$$

This is consistent with the Joule's hypothesis of preferential hydride ion attack at the N(8) position of the pterin ring (Scheme II-1), as compared to the N(5) position; x-ray structural studies have verified that the pyrazine ring is the reaction locant of such a reduction process.[22 , 23] Actually, several authors have pointed out the greater stability of the 7,8- dihydro pterin among other possibilities.[9 – 11,13,146,147] Figures II-16(a) and 16(b) represent the $NH_2(2)$ and $CH_3(7)$ signals of **1** (Scheme II-1) and **3** (Schemes II-4 and II-5) respectively. The two separate $CH_3(7)$ signals of **3** at δ 2.639 and δ 2.365 respectively [Figure II-16(b)], indicate the presence of two forms of this compound in solution on the NMR time scale. Table II-6 shows a comparison of the two above types of ^1H NMR signals, along with the δ (ppm) values. The higher Δ (δ, ppm) value for the $NH_2(2)$ signal with respect to that of the $CH_3(7)$ signal (average value), indicates better electron withdrawal from the pyrimidine ring through complex formation; this inference is consistent with the x-ray structural data of **2** as well as those of a few other complexes of **1** .[17a – 17e]

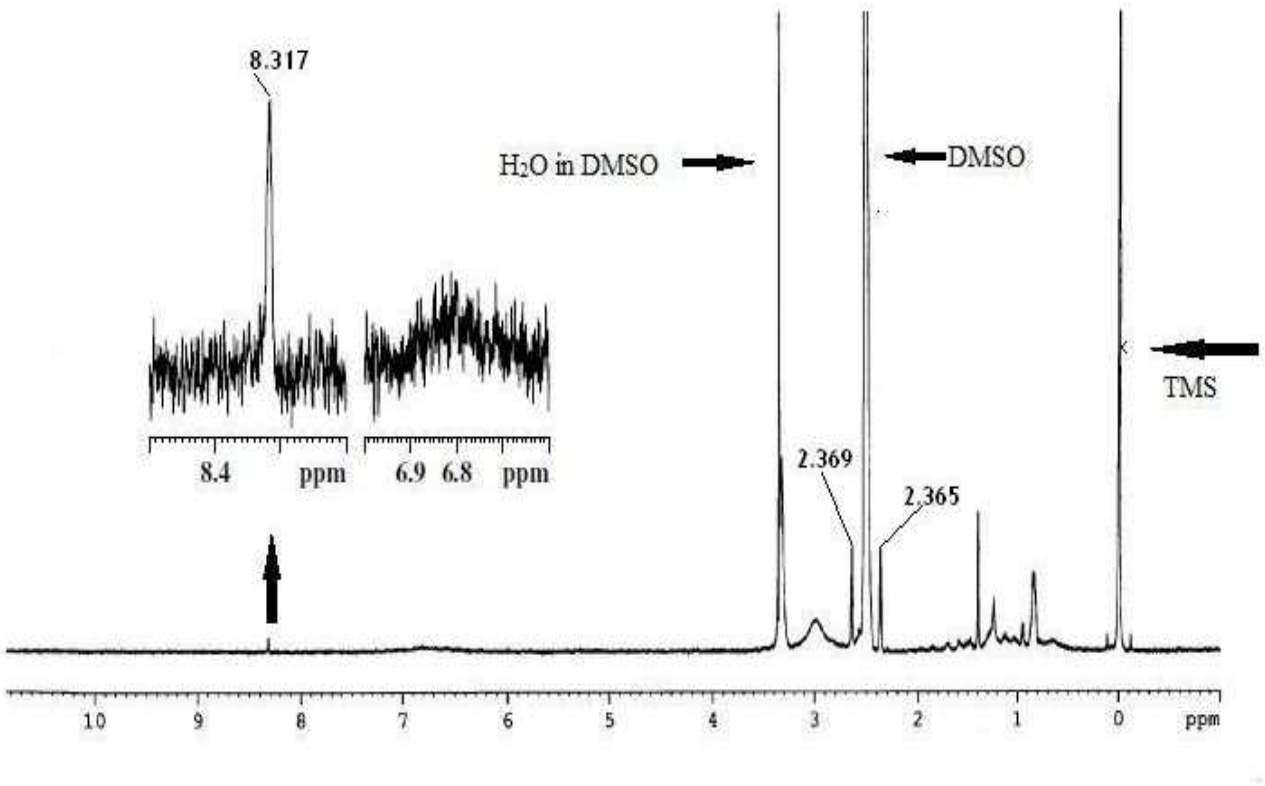

Figure II-15. The 500 MHz ^{1}H NMR spectrum of **3** in DMSO-d_6, with expansion of a few specific regions.

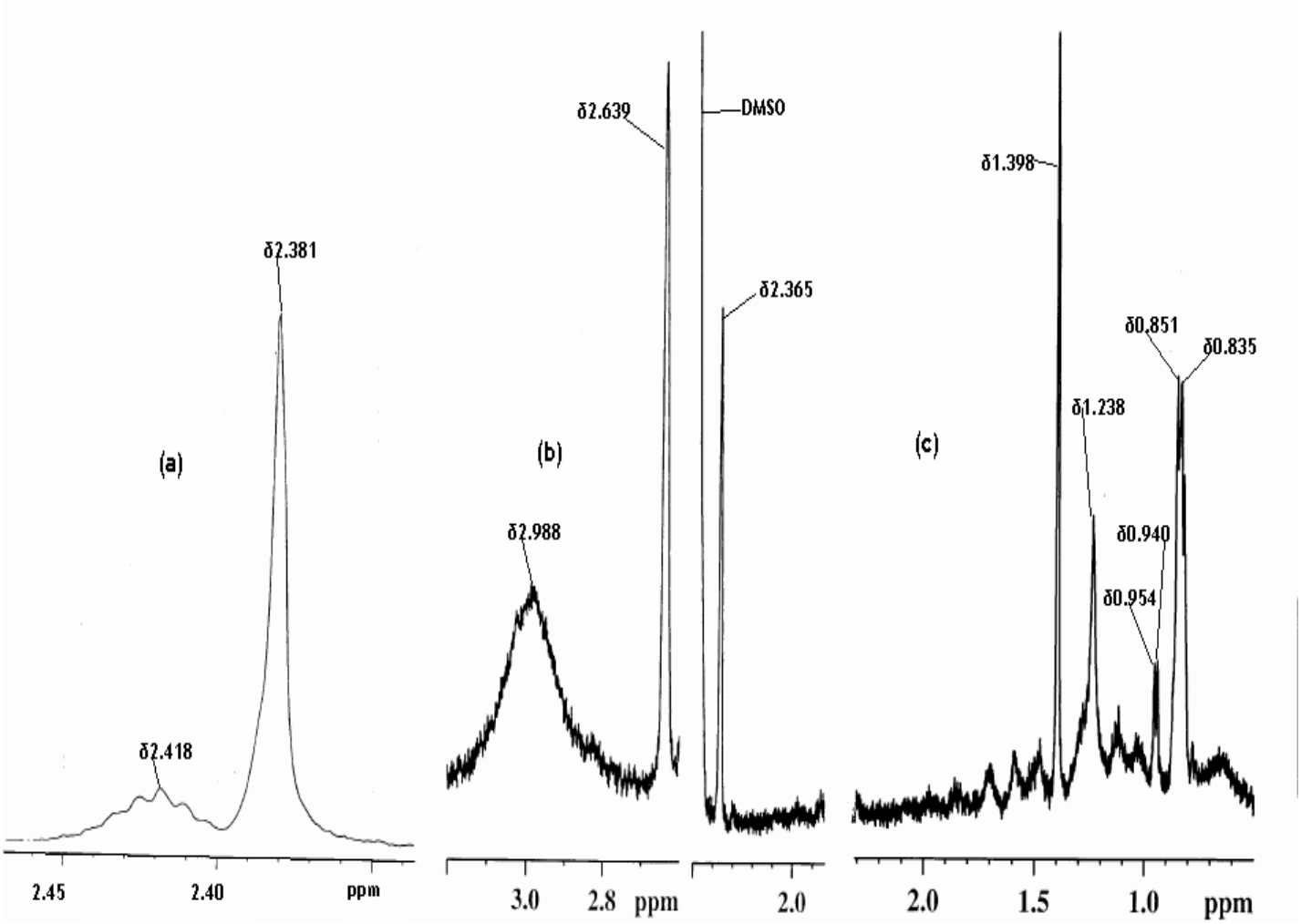

Figure II-16. The 300 MHz ^{1}H NMR spectrum of **1** in NaOD/D_2O(a) ; (b) and (c) represent selected parts of Figure II-15 on expanded scale, highlighting the ^{1}H NMR spectral features of **3**.

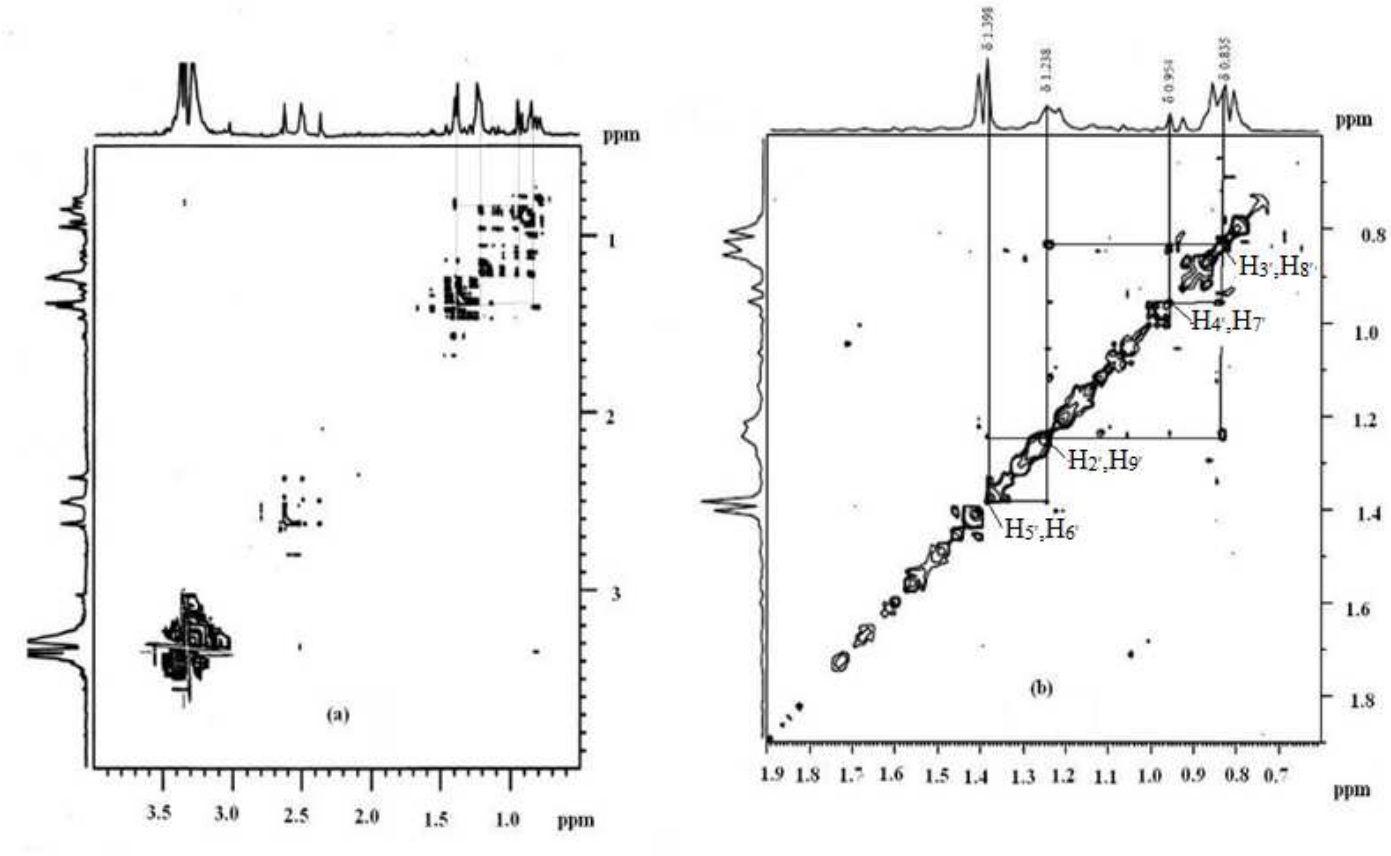

Figure II-17. The 500 MHz 2-D NMR spectrum of **3** (DMSO-d_6); (a) represents the region δ4.0 – 0.5; (b) represents the phen (Scheme II-2) protons signals along with assignments.

Table II-6. Comparison of characteristic ^{1}H NMR signals (δ, ppm) of **1**(Scheme II-1) and **3**(Scheme II-5) along with the corresponding Δ (δ,ppm) values.

Compound	NH_2(2)	CH_3(7)
1	2.418(w,br)	2.381(s,s)
3	2.988(br,s)	2.365(s,s)* 2.639(s,s)*
Δ(δ3 – δ1)	0.57	0.121

***** Two separate CH_3(7) signals correspond to the two separate forms of **3** in solution on the NMR time scale. w, br = weak, broad; s,s = sharp, singlet; br, s = broad, singlet.

The ^{1}H NMR signals of the intra- and extraspheric aquo groups of **3** (Figure II-15), nearly merge with that of the dissolved water (δ 3.35) of DMSO-d_6 .[21] The ^{1}H NMR signals appearing in the region δ 2.0 – 0.5 for **3**(Scheme II-5) [Figure II-15, shown on an expanded scale in Figure II-16(c), together with the 2-D NMR data in Figure II-17], are caused by the protons of its phen residue (Scheme II-2), as elucidated below. Figure II-18 shows the ^{1}H NMR spectral data (both 1-D and 2-D) of 1, 10-phenanthroline monohydrate (phen) in DMSO-d_6, along with the assignments.[39] The phen ligand (Scheme II-2) consists of four magnetically equivalent pairs of protons, e.g., $H_{2'}$ and $H_{9'}$; $H_{3'}$ and $H_{8'}$; $H_{4'}$ and $H_{7'}$ as well as $H_{5'}$ and $H_{6'}$. Among them, $H_{2'}$, $H_{3'}$ and $H_{4'}$ [or $H_{9'}$,$H_{8'}$ and $H_{7'}$] form an ABX or better an ABC system, with the chemically equivalent $H_{5'}$ and $H_{6'}$ protons showing no spin-spin splitting, like those of hydrogen, methane or benzene.[40] For **3** this singlet signal [of $H_{5'}$ and $H_{6'}$] appearing at δ 1.398 [Figure II-16(c)], has

been used here as a point of entry into the present ^{1}H-^{1}H COSY spectra [Figure II-17 (a) and (b)], so that the correct information could be gleaned from them.[21]

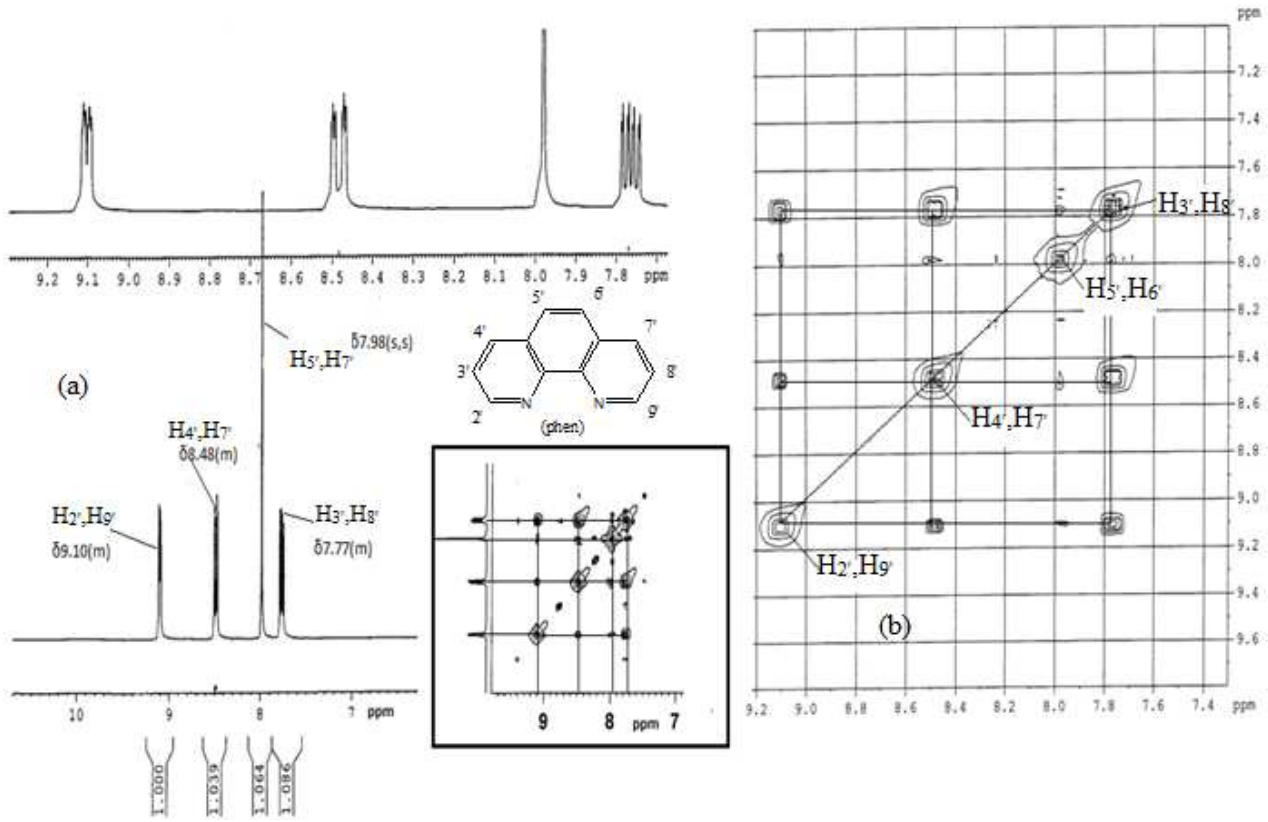

Figure II-18. (a) The 300 MHz ^{1}H NMR spectrum of 1, 10-phenanthroline monohydrate in DMSO-d_6. The inset shows the expanded view of the spectrum as well as the corresponding 2-D ^{1}H-^{1}H cosy spectrum (partly symmetrized). (b) The expanded 2-D ^{1}H-^{1}H cosy spectrum (symmetrized) indicates the assignment of the phen proton signals on the basis of spin-spin interaction and arguments[39,43].

On comparing the 2-D NMR data of **3** in Figure II-17, especially that in Figure II-17(b) with that of phen (Figure II-18), it is evident that apart from the above–mentioned singlet signal at δ 1.398, the spin – spin interactions (in terms of cross peaks) among the three remaining proton pairs help

their unambiguous assignments at δ 1.238 [$H_{2'}$, $H_{9'}$], δ 0.954 [$H_{4'}$,$H_{7'}$]and δ 0.835 [$H_{3'}$,$H_{8'}$] respectively. Just like the CH_3(7) proton signals [Figure II-16 (b)], some of the phen protons are characterized by two sets of signals [Figure II-16 (c) and Figure II-17 (b)], thereby augumenting the inference about the existence of **3** in two forms in solution.

Finally, the chemical shift region (δ2.0-0.5) of the phen proton signals of **3** needs a special mention. Either for the free phen ligand or in complexes where this ligand exhibits different coordination modes, the relevant proton signals appear in the regions δ9.2-7.7 (Figure II-18) and δ10.5-7.7 respectively[39,42,43]. Such exceptionally large lower frequency shift (i.e., shielding by δ 7.8-6.5) in **3**, could be interpreted only in terms of the ring current effect of its two pterin ligand residues which are disposed orthogonally [Schemes II-5, II-5(a)] with respect to the bridging phen ligand[20,40]. X-ray structural data of **2** (Figure II-3) supports such a mutually perpendicular disposition of the phen and pterin ligand residues here.

Circular dichrosim spectroscopy

The above aspect about the asymmetry of the coordination environment, could be further rationalized in terms of the CD spectra [Figure II-19(a) and (b)] of **2** and **3**. **2** shows only weak CD spectral response over the region 300-850 nm. On the other hand, the CD spectrum of **3** consists of a negative Cotton effect at 382 nm associated with a LMCT band; besides this, two broad CD bands associated with shoulders at 460 nm and 732 nm respectively, characterize the MLCT transitions (Scheme II-9). The latter type of transitions could not be located in the UV-VIS spectral data (Table II-5). It can be inferred that the distinct CD spectral features of **3** reflect greater asymmetry of its binuclear μ-phen type coordination environment.[41]

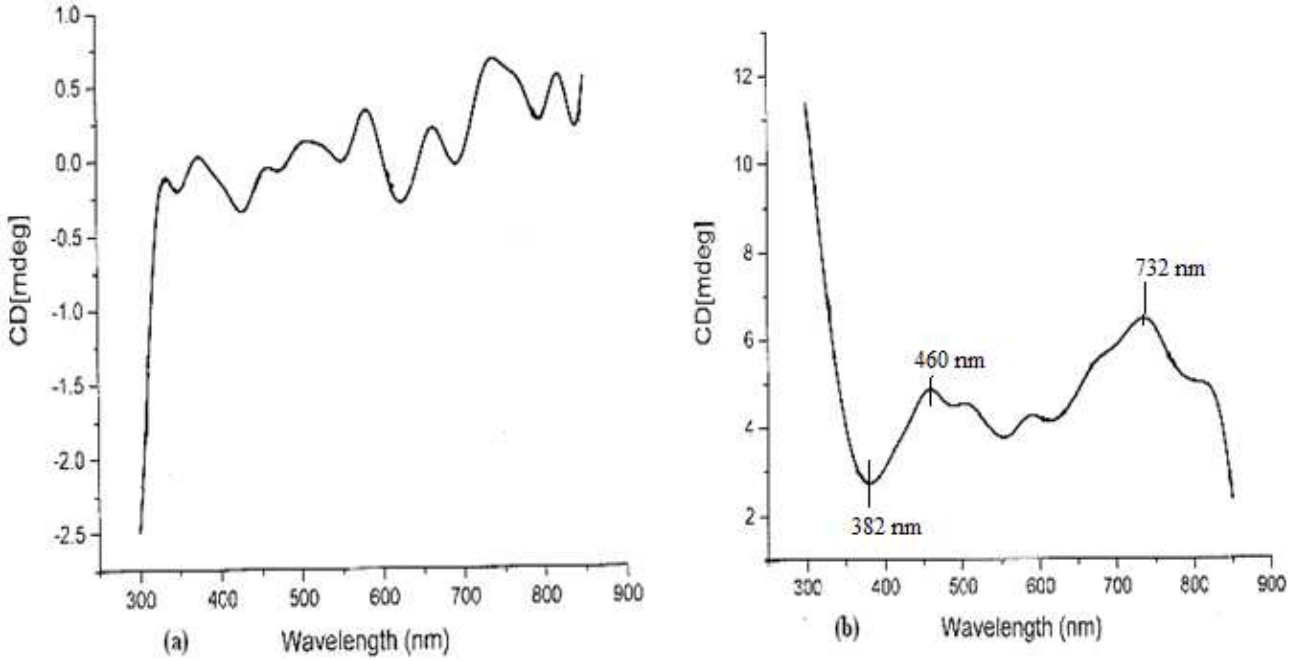

Figure II-19. CD spectral response in CH_3OH of (a) **2 (**($9.3x10^{-4}$ M); (b) **3** ($1.1x10^{-3}$M).

Cyclic Voltammetric Studies.Cyclic voltammetry data of **2** and **3** are presented in Table II-7 as well as in Figures II-20 and II-21. Although the present pterin ligand (**1)** is characterized by a single irreversible reduction peak (E_{pc}) at -418 mV (ca. $1x10^{-3}$mol dm^{-3} in aqueous NaOH medium, pH ca.10 with 0.1M mol dm^{-3} KNO_3; scan rate, 100 mVs^{-1}), the relevant complexes (**2**, **3**) display metal-centred quasi-reversible electrochemical behavior, throwing light on their structure –electrochemical response correlation. Redox reactivities of these complexes studied using UV-Vis spectroscopy as discussed later, corroborate this aspect; for example, the time-dependent spectral curves (Figure II-22) for the $NaBH_4$ reduction of the aquous alkaline solution

of the pterin ligand (**1**) are devoid of any isosbestic point, while such responses of both **2** and **3** towards different redox reagents, do possess such an attribute (Figure II-24 and Figure II-26).

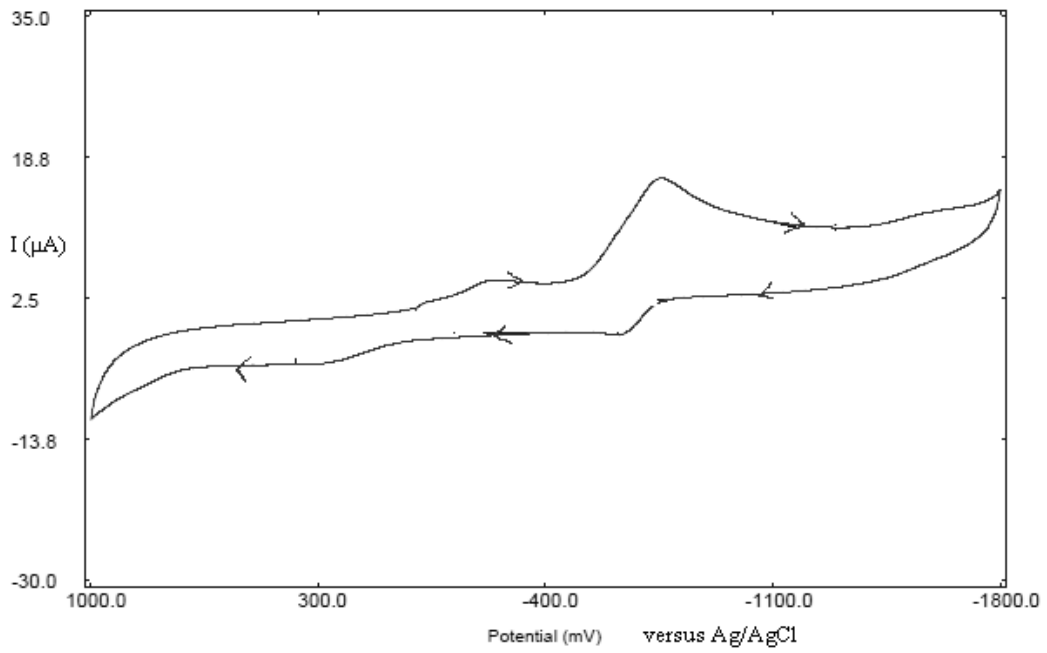

FigureII-20. Cyclic voltammetry data of **2** in DMSO (0.1M TBAP; scan rate, 100mV s^{-1}).

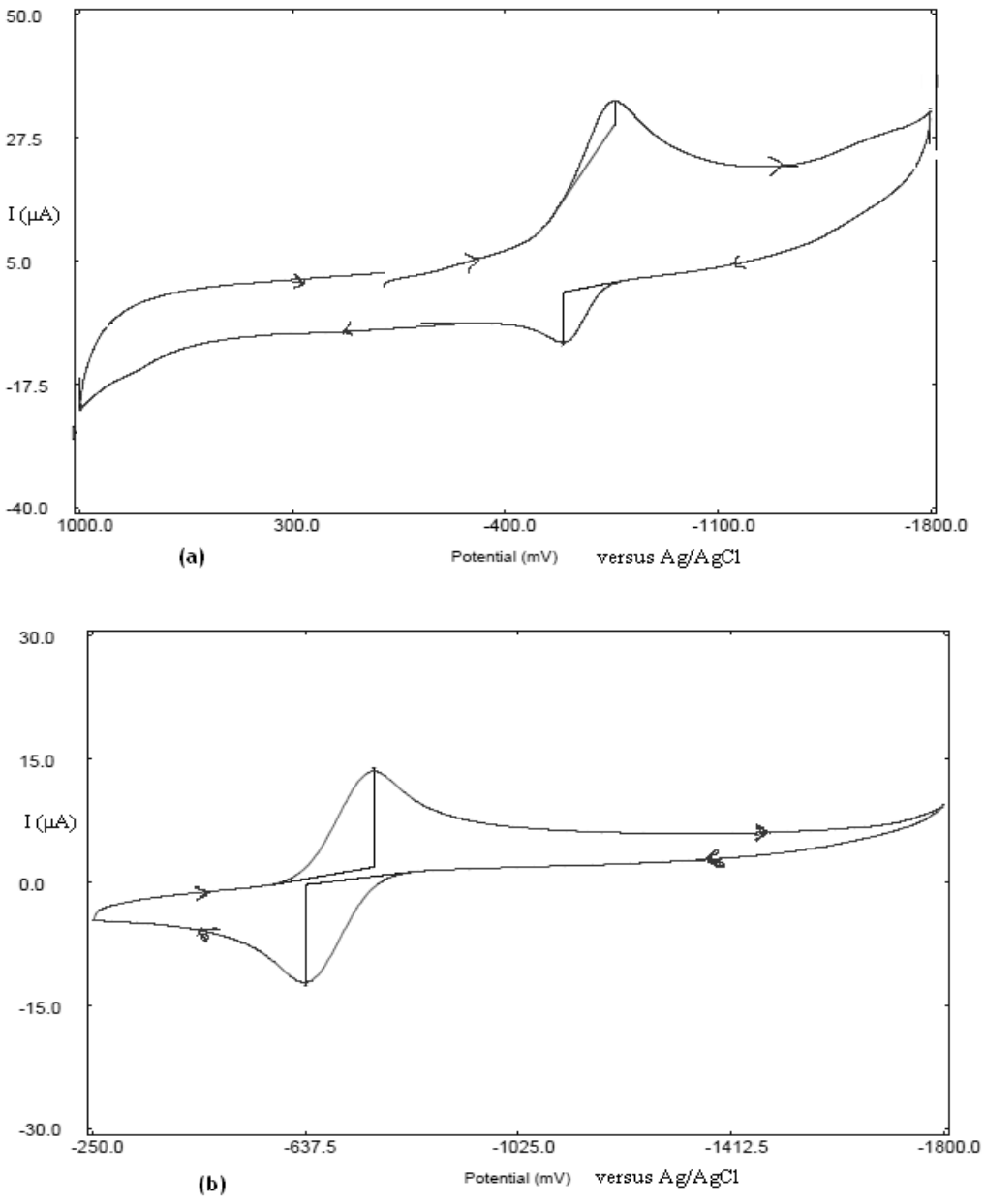

Figure II-21. Cyclic voltammetry data of **3** in DMSO (0.1M TBAP) (a) the potential scan starts from 0 mV and terminates here; scan rate, 300mVs^{1}; (b) the potential scan starts from – 1800 mV and terminates here; scan rate, 150 mVs^{-1}.

Table II-7. Cyclic voltammetry data[a] of the copper complexes **2** and **3** characterizing the process

$$Cu^{2+} + e' \rightleftharpoons Cu^{+}$$.

Complex	E_{pc}(mV)	E_{pa}(mV)	E_0'(V)[b]	ΔE_p(mV)	i_{pc}/i_{pa}
2[d]	-760	-623	-0.691	137	1.2
3[e]	-750	-597	-0.673	153	0.92
3[f]	-762	-637	-0.699	125	0.97

[a] Cyclic voltammetry versus Ag/AgCl using glassy carbon working electrode in DMSO/0.1 mol dm^{-3} TBAP.

[b] $E_0' = 0.5 (E_{pc} + E_{pa})$, where E_{pc} and E_{pa} are the cathodic and anodic peak potentials respectively.

[c] $\Delta E_p = E_{pc} - E_{pa}$.

[d] The potential scan starts from 0(mV) at a rate of 100 mVs^{-1}.

[e] The potential scan starts from 0 (mV) at a rate of 300 mVs^{-1}.

[f] The potential scan starts from -1800(mV) at a rate of 150 mVs^{-1}.

In addition to the characteristic metal-centred peaks (Table II-7), few ligand – centred peaks may also be identified in Figures II-20 and II-21. For **2** two irreversible ligand reduction peaks (E_{pc}) could be detected at -223 mV and -1589 mV respectively, followed by one ligand reoxidation peak (E_{pa}) at 263 mV. In case of **3** weak signals representing ligand reduction and reoxidation could be detected at -1569 mV (E_{pc}) and 777 mV (E_{pa}) respectively, when the

potential scan starts from and terminates at 0 mV as well as extending from -1800 mV to 1000 mV on either side [Figure II-21(a)]. The above- mentioned ligand-centred peaks in Figures. II-20 and II-21(a) are interdependent, as inferred by Gorren and coworkers, from cyclic voltammetry studies on tetrahydrobiopterin [44]. However, close approach to electrochemical reversibility for the Cu(II)/Cu(I) couple could be achieved for **3** [Figure II-21(b)] without any other signal on the wings over the region -250 to -1800 mV, when -1800 mV is selected as the starting point and terminus of the potential scan. As evident from the ^{1}H NMR data of **3**, this situation corresponds to its assigned form [Scheme II-5, II-5(a)], with Cu(I) centers and the pterin ligand residues in their 7,8-dihydro state. The above metal-centred electrochemical reversibility [Figure II-21(b)] could be realized as chemical reversibility in transferring the reducing equivalents from **3** towards the model substrate bromobenzene (Figure II-26) in presence of $O_{2,}$ converting it into 4-bromophenol, as established through stoichiometric study (vide the experimental section).

From electrochemical studies on Cu(II) chelate complexes Patterson and Holm inferred that electrochemical reversibility ($i_{pc}/i_{pa}\approx1$) and thermodynamic driving force ($\Delta G^{0}= -nFE^{0}$) for the Cu(II)/Cu(I) couple are controlled by different ligand parameters, e.g., rigidity favours the Cu(II) state, while flexibility makes the Cu(I) state more accessible; N,O donor ligands shift the E_0'(V) value towards the negative region (-0.70 to -2.26V), whereas a π-acid ligand like phen helps to achieve a positive E_0' value (e.g., +0.64V), with respect to the Cu(II)(aq)/Cu(I)(aq) couple (E_0'=+0.17V) [45 – 47]. The present E_0' values (Table II-7) represent a possible combination of the two above opposite controlling factors. The relevant E_{pc} or E_{pa} values correspond to one-electron transfer step for **2** and two-electron transfer step for the binuclear species **3** respectively [45, 48].

The close approach to electrochemical reversibility for **3** [Figure II-21(b)] may be ascribed to the ability of the ligand environment to adjust with the stereochemical change accompanying the electron transfer:

$$Cu(II)(d^9) + e' \rightleftharpoons Cu(I)(d^{10})$$

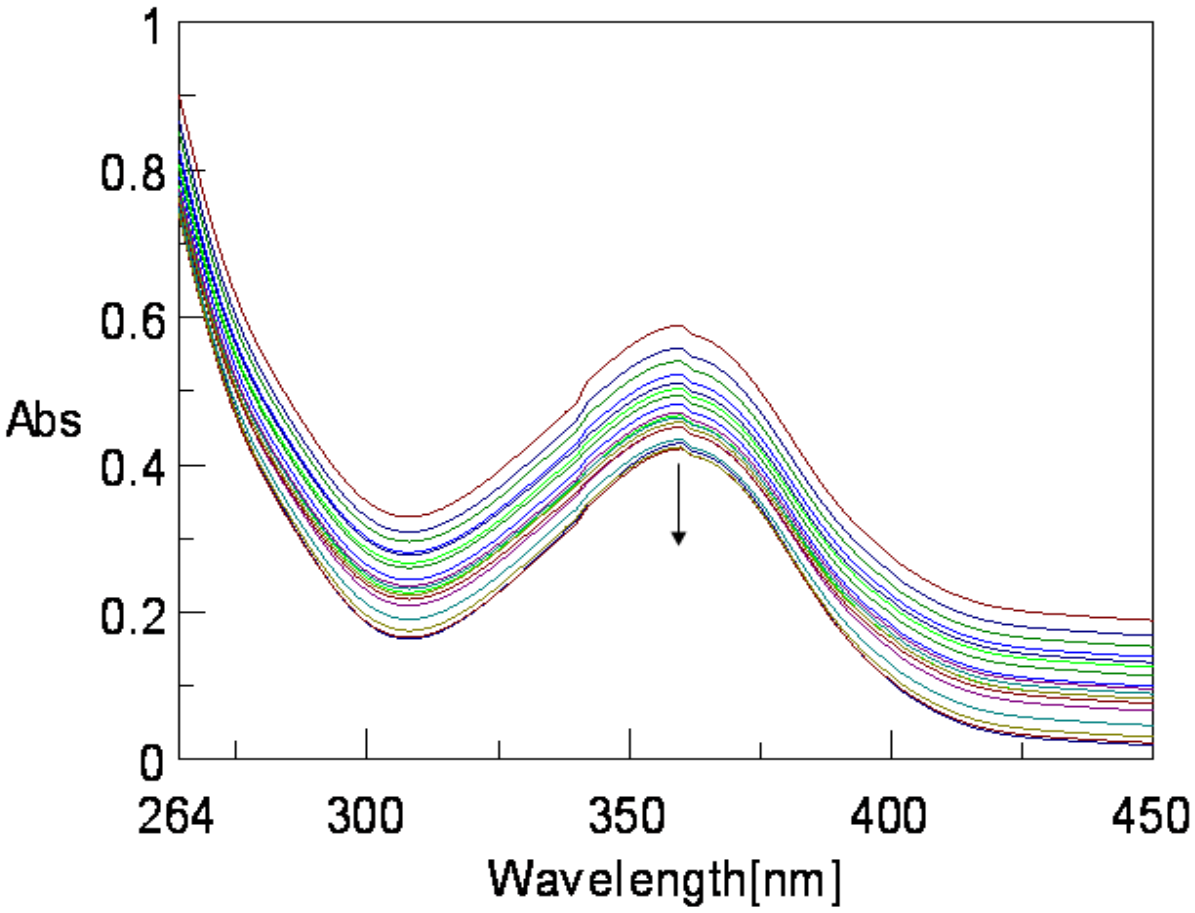

Figure II-22. Absorption spectral changes recorded at 2 min interval during the reaction of **1** ($1.34x10^{-3}$M) in aqueous NaOH solution (1.25 x 10-2M) with $NaBH_4$ (1.35 x 10-2M) at 303K.

Besides this, the (M→L)π bonding ability of the phen moiety (Scheme II-9) also assists this steric adjustments through delocalizing the higher electron density on the Cu(I)(d^{10}) core[32].

Reactivity of 2. 2 possesses an aquo group as well as two redox centres, e.g., the Cu(II) ion and the redox non-innocent pterin ligand residue; thus it provides with an opportunity for exploring its reactivity towards carefully selected group transfer and redox reagents.

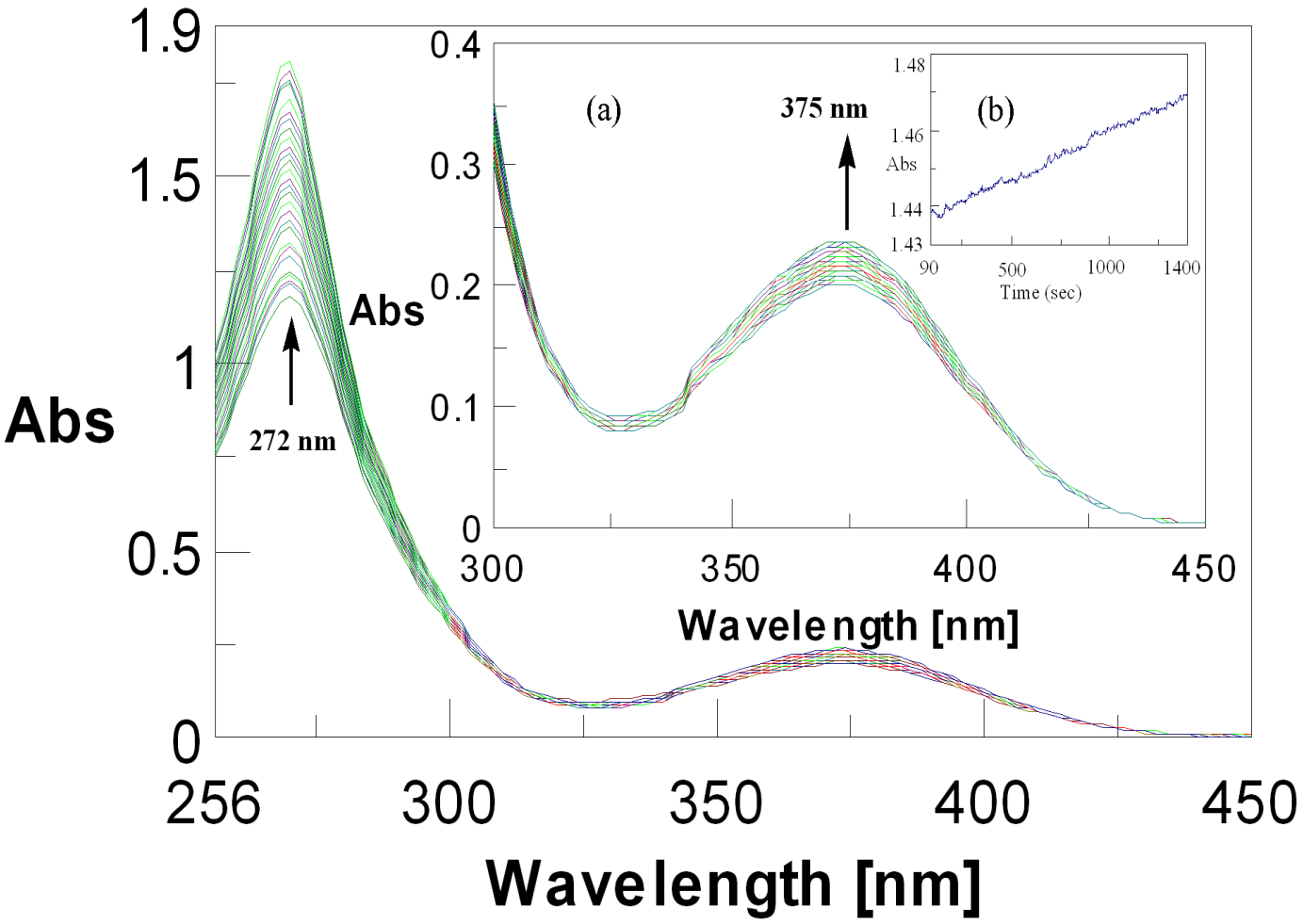

Figure II-23. Absorption spectral changes recorded at 5 min interval during the reaction of **2** (8.9×10^{-5}M) with imidazole (Im) (3.6×10^{-2}M) in CH_3OH at 318K; (a) expanded view (300 –

450nm) of the spectral changes is shown in the inset; (b) the absorbance versus time curve at 375 nm, 318K.

Figure II-23 depicts the absorption spectral changes associated with the reaction of **2** with imidazole in CH_3OH medium at 315K. Imidazole is associated with the histidine residue which is well-known for its avidity towards the first transition metals in the biological system. Stoichiometry of this reaction could be established x-ray crystallographically in the corresponding Ni(II) system [17c]. Kinetics of this reaction was followed at 375nm and four different temperatures in the range 308 – 328 K under pseudo-first-order conditions (keeping ca. 100 times excess of imidazole ligand). Observed rate constants were determined by least square method from the plots of $\log(A_t - A_\alpha)$ versus time, which were linear for 3 half- lives [49,50]. The relevant data are $k_{obs} = 1.4x10^{-2}\ s^{-1}$ and $\Delta S^{\ddagger} = -227.0\ J\ mol^{-1}deg^{-1}$; they are commensurable with a ligand substitution process involving an associative pathway[92,97,98].

Phenylalanine hydroxylase (PAH) is able to activate/hydroxylate the aromatic ring of phenylalanine, converting it into tyrosine, in presence of the cofactor tetrahydrobiopterin (BH_4)[52-55]. One molecule of O_2 is utilized in the reaction; one oxygen atom is inserted into the substrate as an hydroxyl group, while BH_4 supplies the two electrons needed for reducing the other oxygen atom to the level of water. The resulting dihydrobiopterin (BH_2) is restored to its tetrahydro state (BH_4) once again by NADH [10, 51-53]. Although a non- heme iron atom is essential for the functioning of PAH, copper is not needed for this purpose [54].

It is worthwhile to explore the ability of **2** to assimilate reducing equivalents from $NaBH_4$ and the onwards transmission of the same by the reduced compound (**3**), to a model substrate/substrate analogue like bromobenzene in presence of dioxygen [55]. Choice of

bromobenzene for the present study is guided by the fact that the corresponding hydroxylated product (along with any residual portion of the starting material) could be extracted from the reaction medium using pet ether and characterized(vide the experimental section).

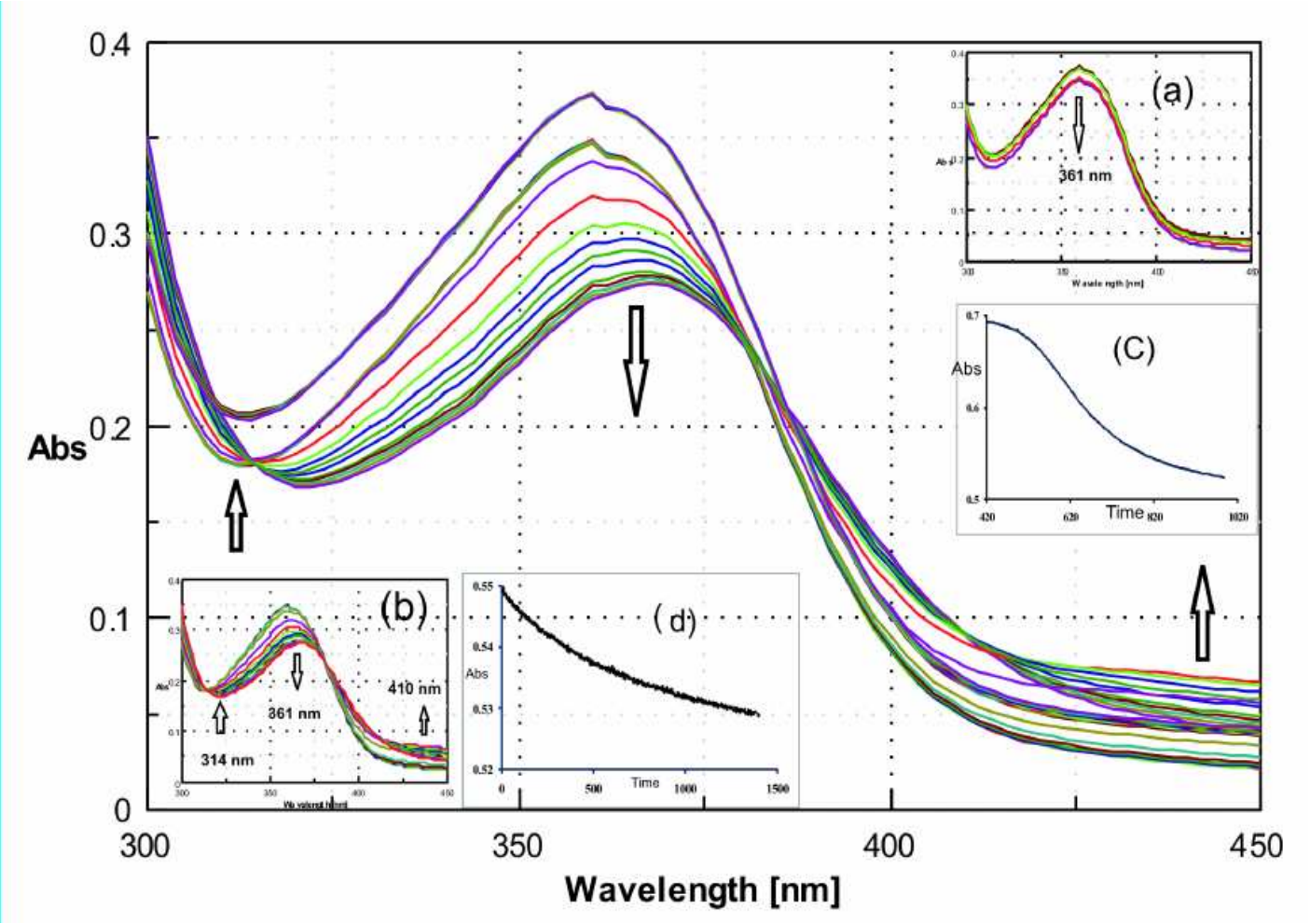

Figure II-24. Absorption spectral changes recorded at 2 min interval during the reaction of **2** (8.9×10^{-5}M) with $NaBH_4$ (6.9×10^{-2}M) in CH_3OH at 298K indicating a composite process which can be separated into two consecutive steps [inset, (a) and (b) respectively]; the step (a) is complete within 35 min; this is followed by step (b) showing three isosbestic points (at 314, 383 and 410 nm) and levelling off after another 25min. The figures (c) and (d) represent the absorbance versus time curves corresponding to steps (a) and (b) respectively.

The reaction of **2** with $NaBH_4$ in CH_3OH (Figure II-24), is essentially a composite process which could be separated electronically into two consecutive steps [Figure II-24(a) and II-24 (b)], in terms of absorption spectral curves. Absence of any isosbestic point in Figure II-24(a) and the presence of such an attribute (at 314 nm, 383 nm and 410 nm) in Figure II-24(b), indicate that the corresponding reaction stages occur with and without structural changes respectively. First stage [Figure II-24(a)] of the reaction continues for ca. 35 min and this is followed by the second stage [Figure II-24(b)], which levels off after 25min; these two stages also differ in terms of their absorbance versus time curves [Figure II-24(c) and II-24(d)] as well. Kinetics of these two consecutive steps of the reaction with $NaBH_4$, were followed at 361 nm and four different temparatures in the range 300 – 330K in CH_3OH under pseudo-first order conditions (with a **2** : $NaBH_4$ ratio of 1 : 140) and the relevant kinetic parameters are stated below:

1st stage [Figures II-24(a) and II-24(c)]: $k_{obs} = 3.8x10^{-3}\ s^{-1}$; $\Delta S^{\ddagger} = -158.0\ J\ mol^{-1}deg^{-1}$;

2nd stage [Figures II-24(b) and II-24(d)]: $k_{obs} = 1.3x10^{-2}\ s^{-1}$; $\Delta S^{\ddagger} = -149.0\ J\ mol^{-1}deg^{-1}$.

As par the negative $\Delta S^{\ddagger}$ values, the transfer of reducing equivalents from $NaBH_4$ to **2** , is an associative process. Figures II-22 and II-25 represent the absorption spectral changes undergone by **1** and phen respectively, on addition of $NaBH_4$ in CH_3OH medium over the relevant spectral region; while phen is essentially insensitive to reduction, the pterin ligand undergoes a definite reaction, with its pyrazine ring being responsible for the reduction [22,23].

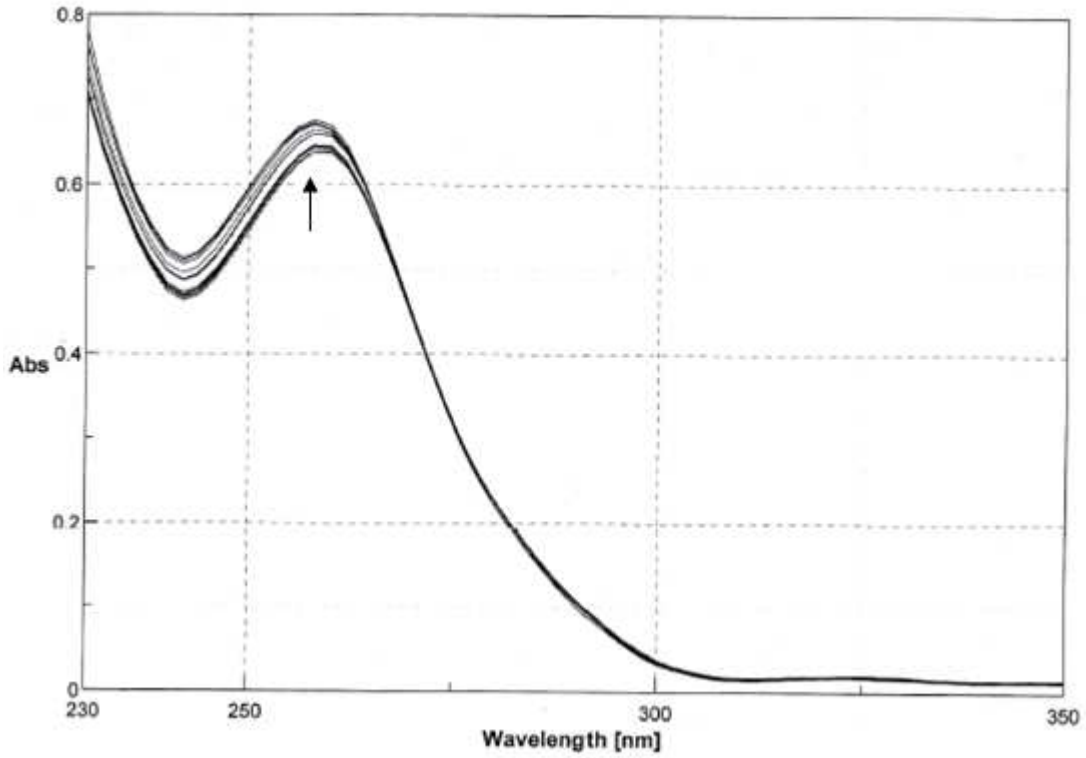

Figure II-25. Absorption spectral changes recorded at 2 min interval during the reaction of 1, 10-phenanthroline monohydrate (phen) (1.25 x10^{-3}M) in CH_3OH at 303K with $NaBH_4$ (1.35 x 10^{-2}M).

Stoichiometry of the above reaction (Figure II-24) could be established through isolation of the $NaBH_4$ reduction product of **2**, i.e., **3** (vide the experimental section for details) and characterizing it. As already pointed out, it is a binuclear Cu(I) complex with the pterin ligand residues in the 7,8-dihydro state [Schemes II-4 and II-5, II-5(a)] and is able to display near reversible electrochemical behavior [Figure II-21(b)] under controlled conditions. Steps leading to the formation of **3** are elucidated below.

Thermodynamic aspects of the reactions of 2 with $NaBH_4$. Cyclic voltammetry data of **2** (Table II-7) indicate an E_0' value of -0.69V for the Cu (II)/Cu(I) couple. The possible E_0' value

for $NaBH_4$ at different pH ranges has received much attention; close to the neutral medium an E_0' value of -0.75V would be a reasonable choice [56-58,161]. Using the above data, an E_{cell} value ($E_{cell} = E_1 - E_2$) of 0.06V is obtained for the Cu(II) + e′ → Cu(I) reduction step in **2** [59]. Again in the light of the ligand reduction peak (E_{pc}) at -0.223V for **2** (Figure II-20), an E_{cell} value of 0.527V is indicated for the reduction of the pterin ligand residue; thus the latter reduction step is thermodynamically more feasible ($\Delta G^0 = -nFE_0'$).

Now utilizing the reducing equivalent flow scheme in the PAH system by Chen and Frey as well as the E_0' values of 0.207V and 0.174V for the iron centre in PAH and the BH_4/BH_2 couple respectively (B = biopterin) by Martinez and coworkers, an E_{cell} value of 0.033V may be calculated for the conversion: phenylalanine + BH_4 + O_2 → tyrosine + BH_2 + H_2O [60 – 62]. In nature the pterin cofactor is regenerated ($BH_2 \rightarrow BH_4$) by NADH ($E_0' = -0.32V$), suggesting an E_{cell} value of 0.494V for the regeneration step [53]. Such estimated E_{cell} values for the PAH system fall within a range, comparable to those of the **2** - $NaBH_4$ reaction system as above.

A closer look may be taken at Figure II-24 in the light of the above guidelines and Schemes II-4, II-5 and II-6 for understanding this reduction reaction. In terms of the aforesaid thermodynamic driving forces ($\Delta G^0 = -nFE_0'$), the relevant time - dependent absorption spectral changes could be differentiated into two distinct types [Figures II-24(a) and II-24(b)], e.g., without and with isosbestic points. In other words, the transfer of reducing equivalents to two different redox centres covalently linked within the same molecule (**2**), may be visualized on the time scale of electronic spectroscopy. As par the above thermodynamic driving forces the first step [Figure II-24(a)] without any isosbestic point represents the transfer of reducing equivalents to the pterin ring, followed by the formation of a putative Cu(II) intermediate **2′** (Scheme II-6) ; the next step [Figure II-24(b)] characterized by isosbestic points reflects the reduction of the

metal centres of **2′**, associated with the transformation, **2′ → 3** . As evident from the $k_{obs}(s^{-1})$ data stated earlier, the second step is ca. 3 times faster than the first one. This is consistant with the cyclic voltammetry data of **3** [Figure II-20(b)], indicating a close approach to electrochemical reversibility for the corresponding metal-centred redox process

$$Cu(II)(d^9) + e' \rightleftharpoons Cu(I)(d^{10})$$.

Reactivity of 3 with bromobenzene and dioxygen. For exploring the redox ability of **3** in transferring reducing equivalents, its reactivity towards bromobenzene (a model substrate for exploring PAH type activity) in presence of dioxygen has been studied [55]. Figure II-26 shows a clean reaction with two isosbestic points (314 nm and 396 nm) and the arrows indicating movements of the absorption spectral curves, represent opposite behavior as compared to those in Figure. II-24(b). Taken together, the two figures [Figure. II-24(b) and Figure. II-26], represent the response of **2** towards a reducing agent like $NaBH_4$, leading to the formation of **3** and the ability of **3** in transferring the reducing equivalents to bromobenzene in presence of O_2, respectively. Kinetics of the latter reaction (Figure II-26) was followed at 372 nm and four different temperatures (range 300-330K) in CH_3OH saturated with O_2 under pseudo-first-order conditions (with a **3**: bromobenzene ratio of 1:140) and the relevant data are indicated below:

$$k_{obs} = 2.9x10^{-2}s^{-1} ; \Delta S^{\ddagger} = - 196.0 \text{ J mol}^{-1}\text{deg}^{-1}.$$

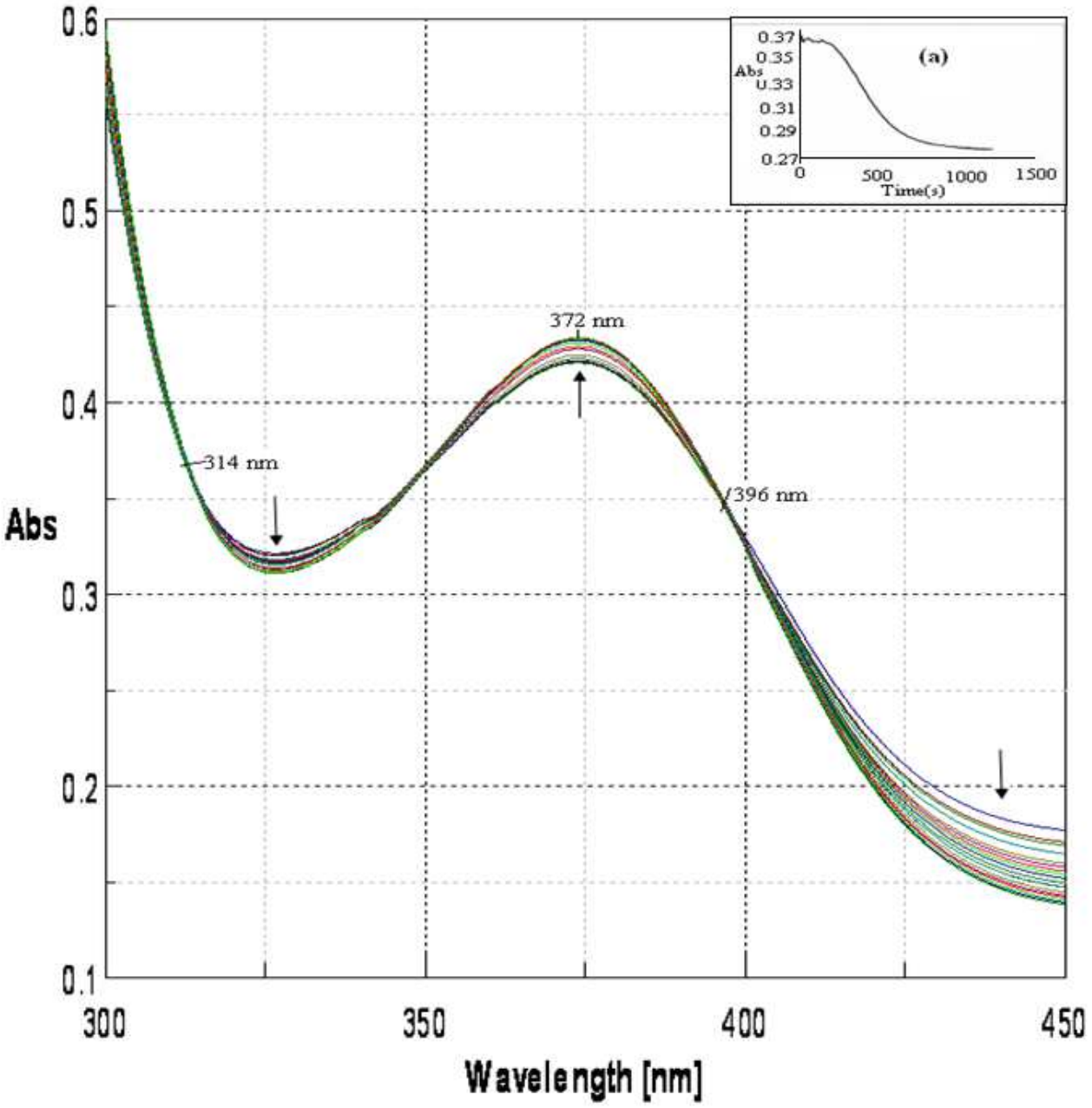

Figure II-26. Absorption spectral changes recorded at 5 min interval during the reaction of **3** (1.0×10^{-4}M) with bromobenzene (1.9×10^{-2}M) in CH_3OH saturated with O_2 at 300K; (a) the absorption versus time curve at 372 nm, 303K.

They indicate an associative (Scheme II-7) process with a rate constant comparable to that of the reaction represented by Figure II-24(b). Stoichiometry of this reaction[Figure II-26; Scheme II-8(b)] was checked through its repetition on the preparative scale and isolating / characterizing 4-bromophenol and **2** as the products (vide the experimental section)[55].

Aerial Oxidation of 3. Again, when **3** is left exposed to air in the absence of a substrate (e.g., bromobenzene), it is reconverted to **2** [Scheme II-8 (a)], as already established x-ray structurally[17b]. Most likely H_2O_2 evolution accompanies this transformation, associated with one two-electron transfer step from the binuclear Cu_2(I) centre of **3**, as indicated below [48,63]:

$$O_2 + 2H^+ + 2e' \rightleftharpoons H_2O_2 \; ; \; E_0' = 0.70 \text{ V}.$$

It helps to overcome the barriers associated with dioxygen reaction; the corresponding one-electron reduction is difficult ($E_0' = -0.16$V) due to the exchange stabilization of the high-spin configuration ($^3\Sigma_g$) [67].

Reactivity and Electronic Structures of 2 and 3. Viewed in the perspective of Scheme II-8 (a composite of Schemes II-6 and II-7), it is evident that the transfer of reducing equivalents(from $NaBH_4$) to **2** converts it to the binuclear species **3** and further transfer of the same to the O_2/bromobenzene reaction system [Scheme II-8 (b)] restores the original mononuclear species **2**. These steps are associated with structural rearrangements involving the copper centres and an important role is played by the phen residue of **3** during the conversion:

$$2Cu(II) + 2e' \rightleftharpoons 2Cu(I) \; .$$

Recent x-ray structural study of the coupled binuclear copper enzyme tyrosinase reveals apparent mobility in copper binding modes, assisting the substrate binding orientation. But here six conserved histidine residues are able to preserve the binuclear active site of this enzyme [68 – 71].

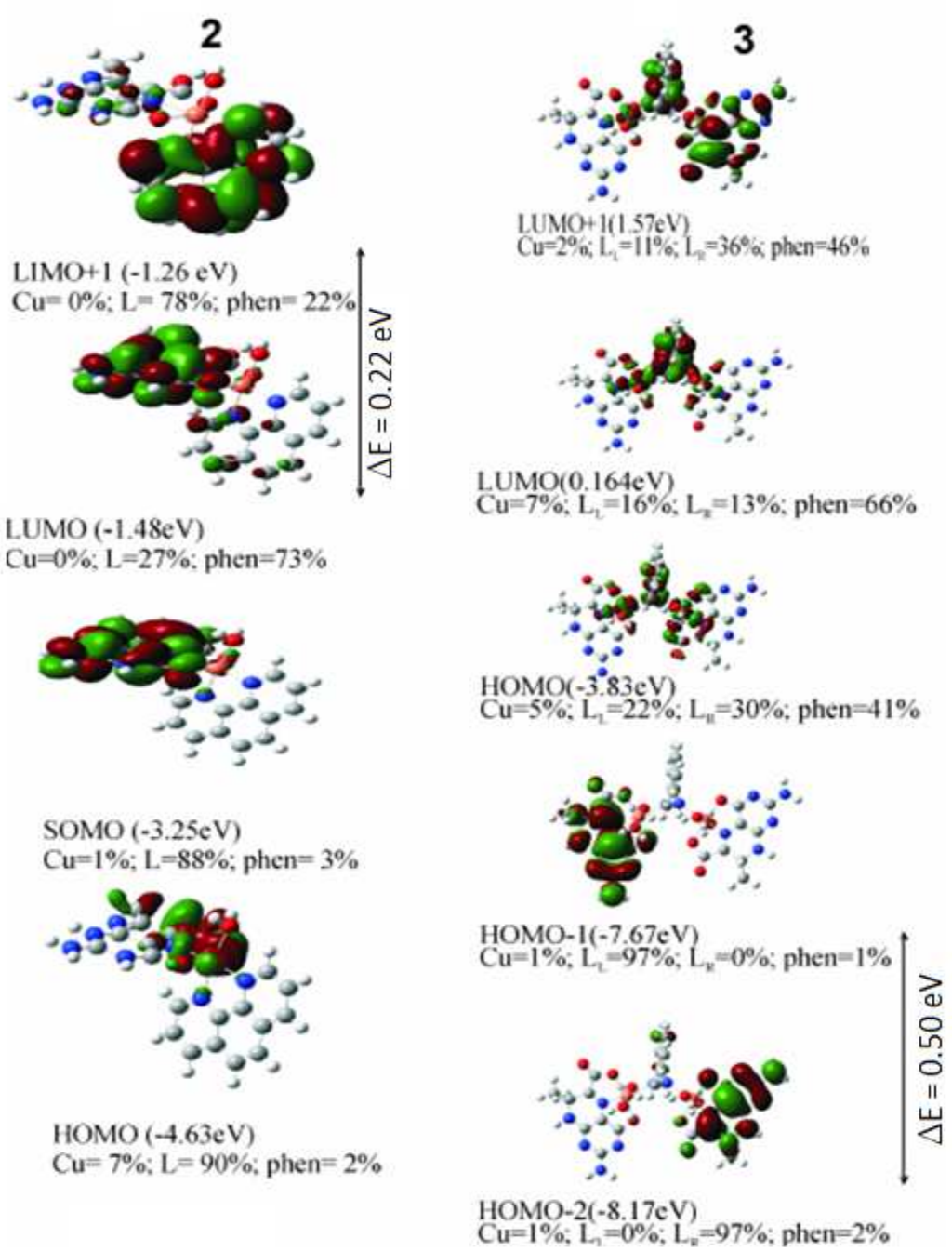

Figure II-27. Frontier molecular orbitals of **2** and **3**, showing their energies (eV) and compositions (%). The notations L_L and L_R represent the two pterin ligand residues of **3** [Scheme II-5, II-5(a)].

Further insight into the electron transfer process of **2** and **3** could be obtained from the frontier MO energy levels and their compositions (Figure II-27) obtained by DFT calculations[154-159]. Reliability of such a theoretical model is evident from its ability to interpret the chirality of **3** [Figure II-19(b)] in terms of unequal occupancies of the two pterin residues (L_L and L_R) at the HOMO-1 and HOMO-2 levels respectively (Figure II-27); this creates an asymmetry about the phen residue (of **3**), which survives to a lesser extent even upto the HOMO level. The small band gap (0.5eV) between the HOMO-1 and HOMO-2 levels of **3** possibly facilitates its one-step reaction with the O_2/bromobenzene mixture [Figure II-26 and Scheme II-8(b)]; this step involves oxidations of both the metal [Cu(I)] and pterin ligand (7,8-dihydro form) centres of **3**, leading to the recovery of **2**. On the other hand, **2** is characterized by a even smaller band gap (0.22eV) between its LUMO and LUMO+1 levels (Figure II-27), which can accommodate the reducing equivalents transferred by $NaBH_4$ (Figure II-24; Schemes II- 6,7 and 8).Such transfer of reducing equivalents in the opposite directions for **2** and **3** affects the oxidation states of their metal and pterin centers. Now-a-days synthetic molecules with exceptionally small (<0.5eV) HOMO –LUMO gaps (HLG) are receiving considerable attention due to their interesting electrochemical/redox amphoteric behavior [64 - 66]. Usually in such cases the HOMO – LUMO orbitals are located in different covalently linked centres in a single molecule. Thermo-excited intramolecular electron transfer may occur between two such centres in solution. Perhaps the combination of the redox non-innocent pterin ligand residue with the redox active metal centre [Cu(II)/Cu(I)] in complexs **2** and **3**, helps to achieve such a situation here, associated with the distinct redox activities [Figures II-24 and II-26][9 – 11, 53].

Conclusion

A structurally characterized copper (II) complex (**2**) of a 6-substituted pterin ligand (**1**, Scheme II-1) is able to retain reducing equivalents from $NaBH_4$, leading to the formation of a bimolecular copper (I) complex **3**. The latter is able to convert a model substrate like bromobenzene to 4-bromophenol in presence of O_2 and affording back the original complex **2**. Again, **3** is able to display near reversible electrochemical behavior under a special condition [Figure II-21(b)]. These aspects are summarized in Scheme II-8 and Figure II-28. Such reactivities have been elucidated on the basis of physico-chemical studies and further rationalized in the light of electronic structures (DFT methods).

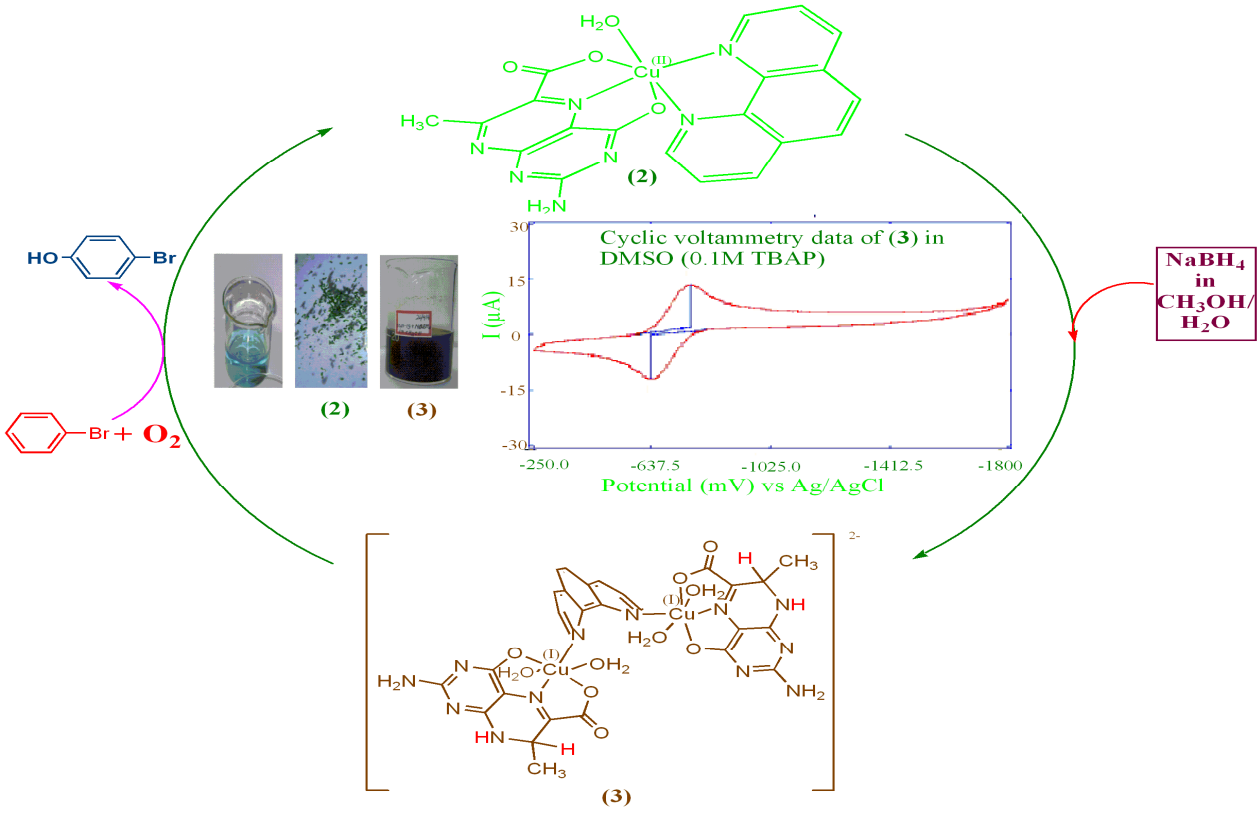

Figure II-28. A summary of the chemical and electrochemical reactivities of **2** and **3**.

That is, small band gaps (<0.5 eV) between the relevant frontier orbitals are responsible for the transfer of reducing equivalents to **2** and their facile release from **3.** Exceptional stability of the coordination geometry around the Cu (II) ion in **2** is indicated, which allows it to survive through different chemical transformation (Scheme II-8). A combination of the redox non-innocent tridentate pterin ligand (**1**) and the π-acceptor ancillary ligand phen around the copper centre with its two closely related oxidation states [Cu (II)/ Cu (I)], possibly confers this unique redox flexibility.